Key Points:
- Tasmantid Seamount morphology governed by structural inheritance from Tasman spreading center, despite eruption >20 Ma after spreading ceased
- This morphological dependence, low mass-wasting rates, and evidence of dense intrusive cores suggest a relatively weak Tasmantid plume
- T_e measurements suggest lithosphere is heavily faulted near ridge-transform intersections, deforming predominantly by brittle yielding

Supporting Information:
- Supporting Information S1

Correspondence to:
F. D. Richards,
frichards@schmidtsciencefellows.org

The Morphology of the Tasmantid Seamounts: Interactions Between Tectonic Inheritance and Magmatic Evolution

F. D. Richards[1,2], L. M. Kalnins[3,4], A. B. Watts[1], B. E. Cohen[5,6], and R. J. Beaman[7]

[1]Department of Earth Sciences, University of Oxford, Oxford, UK, [2]Bullard Laboratories, Department of Earth Sciences, University of Cambridge, Cambridge, UK, [3]Department of Earth Sciences, Durham University, Science Labs, Durham, UK, [4]School of GeoSciences, University of Edinburgh, Edinburgh, UK, [5]Scottish Universities Environmental Research Centre, East Kilbride, UK, [6]School of Geographical and Earth Sciences, Gregory Building, University of Glasgow, Glasgow, UK, [7]College of Science and Engineering, James Cook University, Cairns, Queensland, Australia

Abstract Basement structure is known to exert strong magmatic and morphological control on continental volcanoes, but relatively little is known about the structural control of submarine volcanoes. Here we investigate the morphology of the Tasmantid Seamounts, a >2,400 km long chain of age-progressive intraplate volcanoes, ranging from 56 to 7 Ma. The seamounts are emplaced over the extinct Tasman Sea spreading center, which was active between 84 and 52 Ma. While thick sediment (~1 km) obscures much of the basement, detailed morphological and geophysical analyses of the seamounts reveal a strong correlation between tectonic setting, seamount orientation, and volcanic structure, despite the ≥20 Ma interval between spreading cessation and seamount emplacement. Seamounts emplaced on fracture zones or spreading segment-transform fault inside corners are typically large and elongate. Where original morphology is preserved, they often appear rugged and predominantly fissure-fed. By contrast, comparatively smooth, conical seamounts with isolated dike-fed flank cones are often found midsegment and at outside corners. Volcanic fabrics also align closely with the expected principal stress directions for strong mechanical coupling across transform faults. This behavior suggests the lithosphere is dissected by numerous deep faults, channeling magma along preexisting structural trends. Generally, low effective elastic thicknesses (<10 km) and lack of correlation with plate age at emplacement suggest that structural inheritance is also a major control on lithospheric strength near the extinct spreading center. Our study clearly demonstrates that, like in the continents, structural inheritance in oceanic lithosphere can exert significant control on the morphology of submarine volcanoes.

Plain Language Summary The shapes of volcanoes in continental regions can be strongly influenced by faults. These lines of weakness provide a natural pathway for rising magma so that large volumes are erupted along these trends, and volcanoes are often elongated parallel to underlying faults. However, little is known about the effect of faults on submarine volcanoes. Here we use high-resolution ocean depth and gravity data to investigate how faulting influences the structure of the Tasmantid Seamounts, a 2,500 km long chain of underwater volcanoes off the east coast of Australia. We find that seamount shapes are strongly influenced by faults that formed when Australia and New Zealand rifted apart, tens of millions of years before the volcanoes formed. The mechanical strength of the crust and mantle beneath the seamounts is also far weaker than expected due to the faulting. Finally, much of the magma making up the volcanoes never reached the surface and instead solidified below the seafloor. This suggests that the hot region in the mantle causing the volcanoes to form was not very strong compared to places like Hawaii or Iceland. This study shows that, like in the continents, preexisting faults can have a profound effects on the structure of submarine volcanoes.

1. Introduction

The major control exerted by preexisting crustal and lithospheric structure on the location and fabric of volcanism is well documented in continental settings (e.g., Davies et al., 2015; Ebinger & Sleep, 1998; Valentine & Krogh, 2006). In the oceans, seamounts formed at active spreading centers also show significant lithospheric control, with volcanic rift zones and elongation directions heavily influenced by ridge structure and the state of stress in the lithosphere (Dick et al., 2003; Hekinian et al., 1999). However, structural inheritance is generally

considered of secondary importance in intraplate oceanic settings. Although Michon et al. (2007) attribute the preferential alignment of volcanic structures at La Réunion to reactivation of preexisting faults, they suggest this applies only when plate motion is slow.

To investigate how an extinct spreading center's structure influences later volcanism, we examine the central Tasmantid Seamounts. This ≥2,400 km long seamount chain lies off the east coast of Australia and decreases in age from 56 Ma in the north to 7 Ma in the south (Figure 1; Crossingham et al., 2017; Kalnins et al., 2015; McDougall & Duncan, 1988), consistent with northward Australian plate motion over a relatively stationary and localized thermal anomaly in the mantle. It is one of a set of three major subparallel intraplate volcanic trails in the region, together with the continental East Australian Volcanic Chain and the Lord Howe Seamount Chain (Cohen et al., 2013; Johnson et al., 1989).

At several locations, the chain crosses the extinct Tasman Sea mid-ocean ridge and fracture zones (Figure 1), which were active from 84 to 52 Ma (Gaina et al., 1998). The Tasmantids therefore provide an excellent opportunity to explore how inherited structures in oceanic lithosphere can influence the large-scale magma movement and resulting geomorphology of later volcanism. Although plate velocities were modest during active spreading (~10 mm/a, Müller et al., 2008), northward Australian plate motion later accelerated, reaching 40–70 mm/a at various times during the last 30 Ma (Seton et al., 2012), significantly faster, for example, than the motion of the Indian plate during La Réunion volcanism.

Previous work on the Tasmantids has focused on their isotope geochemistry and ages. McDougall and Duncan (1988) used potassium-argon (K-Ar) and total-fusion argon-argon (^{40}Ar/^{39}Ar) dating to demonstrate the chain's southward-younging age progression south of 27.5°S. Eggins et al. (1991) found these samples ranged from tholeiitic to alkali-olivine basalt and, with trace element and isotope data, they interpreted that the magmas represented a mixture of a deep-origin EM1 plume with shallower PREMA or MORB mantle. In geophysics, the Australian Bureau of Mineral Resources 1970–1973 continental margin survey acquired single beam bathymetry, gravity, magnetics, and sparker seismic data along regular east-west profiles spaced 0.5° apart across the Tasman Sea, occasionally crossing one of the Tasmantids (Mutter, 1974; Symonds, 1973). More recent data are limited to several transit crossings acquiring predominantly multibeam bathymetry data.

During voyage TMD2012 (ss2012_v07) on the R/V *Southern Surveyor* from 23 November to 19 December 2012, dredge samples and swath bathymetry, gravity, and magnetic data were collected to create a broad geological and geophysical database from Stradbroke Seamount to Wreck Reefs (Figure 1). We combine these new data with publicly available regional data sets (Beaman, 2010; Exon, Bernardel et al., 2006, Exon, Hill et al., 2006, Symonds, 1973) to quantitatively analyze the seamounts' morphology and determine the major controls on their structure and evolution. Our analysis demonstrates that construction of the Tasmantids and strength of the underlying lithosphere is predominantly controlled by preexisting structures associated with seafloor spreading, despite the Australian plate's rapid motion and the ≥20 Ma between spreading cessation and seamount emplacement. This shows that structural inheritance in oceanic lithosphere cannot be ignored at either slow (Michon et al., 2007) or fast plate velocities and can be an important filter on the surface expression of deeper mantle processes.

2. Data

The Tasmantid voyage TMD2012 acquired 16,000 km^2 of bathymetric data, 7,700 line-km of gravity data, and 35 successful dredges across 16 of the Tasmantid Seamounts (Cohen, 2012). A Kongsberg Seapath 320 GPS and Seatex Motion Reference Unit provided location data that are accurate to ~2 m and heading and ship motion data typically accurate to ±0.025° (Kongsberg Maritime AS, 2004).

2.1. Bathymetry Data

Swath bathymetry data were acquired using a hull-mounted EM300 Kongsberg-Simrad multibeam system and postprocessed using Caris HIPS & SIPS. The velocity structure of the water column was measured by 16 expendable bathythermographs (XBTs) to accurately depth-convert the data set (Cohen, 2012). The EM300 system also collected backscatter data, a measure of acoustic reflectivity that depends on the roughness and hardness of the seafloor. Accuracy was assessed using repeat tracks in a 3 × 3 km area over North Brisbane Seamount, giving a mean error of 1.3 m and an RMS error of ±2.5 m. Seafloor coverage was generally close to 100%, except in rough seas when yaw and pitch exceeded 10%. Bathymetry data were gridded to 30 m using GMT5's `surface` routine (Wessel & Smith, 2013) and combined with the gbr100 V4 grid, which includes the
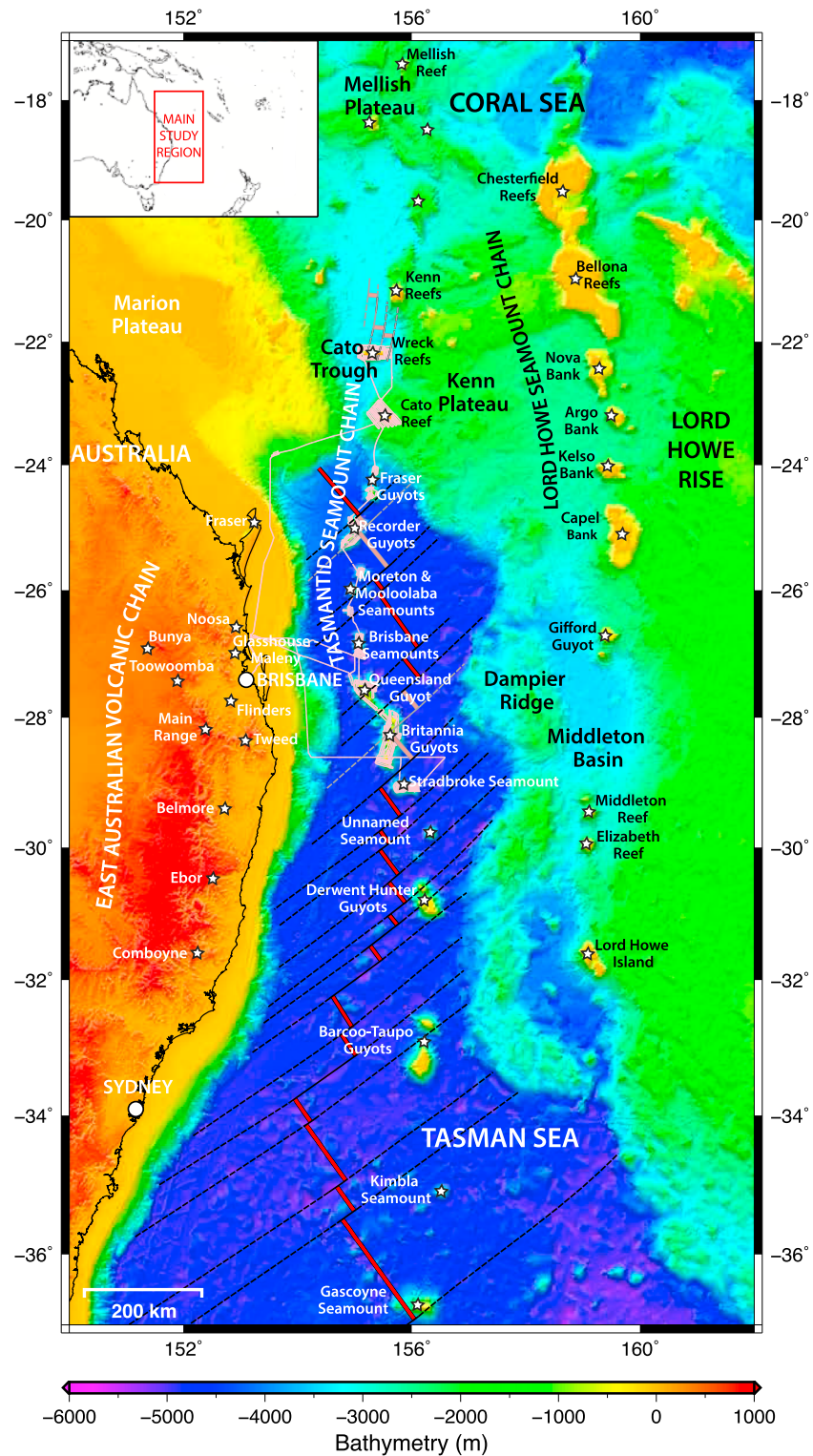
Figure 1. Regional bathymetric map showing the Tasmantid Seamount Chain and its relationship with the extinct Tasman Sea spreading center, inferred from the vertical gravity gradient (Supporting Information Comment S1 and Figure S1; Sandwell et al., 2014). Cato Trough fracture zones and spreading segments after Gaina et al. (1999). White stars = major volcanoes of the East Australian, Tasmantid, and Lord Howe volcanic chains. Thick red and pink lines = Tasman Sea ridge axis; black and gray dashed lines = Tasman Sea fracture zones and transforms; lighter colors indicate less certain locations. Thin pink line = route of voyage TMD2012.
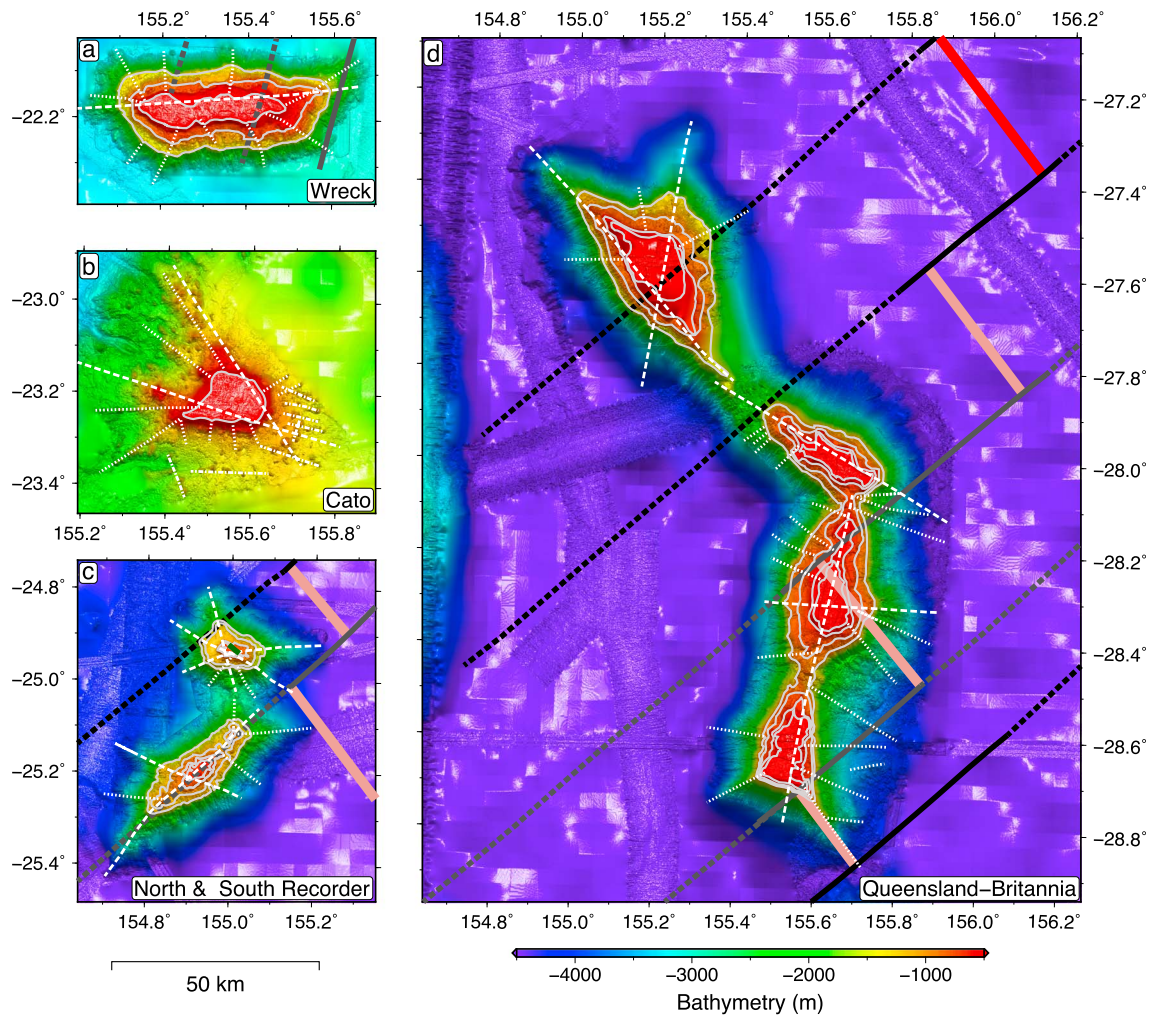
Figure 2. Bathymetry, structure, and tectonic setting of (a) Wreck, (b) Cato, (c) North and South Recorder, (d) Queensland and North, South, and Central Britannia. Extinct ridge segments and fracture zones as in Figure 1; white dashed lines = principal axes of elongation and major volcanic ridges; white dash-dotted lines = lineaments of isolated volcanic cones; white dotted lines = minor volcanic ridges; gray solid lines = wave-cut terraces; dark green solid lines = faults. Scale is 1:750,000. Coordinate values given in meters are eastings and northings for Universal Transverse Mercator zone 56S. Larger maps can be found in Figures S2–S27.

latest available single beam, multibeam, and shallow water satellite and LIDAR bathymetry data sets at 100 m resolution (Beaman, 2010). The gbr100 data set ends at 29.1°S, just south of Stradbroke Seamount, so data from the 0.5 arcminute GEBCO grid (BODC, 2014) were used south of this (Figure 3g).

Survey planning prioritized the upper flanks and non-wave-cut summits of the seamounts to maximize information on volcanic morphology and interseamount variation, achieving almost complete coverage down to ~3,500 m (Figures 2 and 3). Large wave-cut platforms, such as Queensland and Britannia (Figure 2d), and deeper flanks of the seamounts were limited to partial coverage due to the narrower swath width of the EM300 system in these settings. In addition, the summits of Cato and Wreck are active reefs and could not be surveyed by ship; their mapping relies on shallow water bathymetry data (predominantly LIDAR) from gbr100 (Figures 2a and 2b).

2.2. Gravity and Magnetics

Gravity data were collected using LaCoste & Romberg Air-Sea II gravimeter S-040, with measurement locations determined by the ship's differential GPS. Gravity was measured continuously barring shutdowns on 5 December 2012 to replace a flat air-shock and 12–13 December 2012 due to high seas. To correct for instrumental drift and convert the relative gravity data to absolute values, land ties were made before and after the expedition at the 2006 Mount Coot-tha base station (Geoscience Australia #2006910347) in Brisbane,
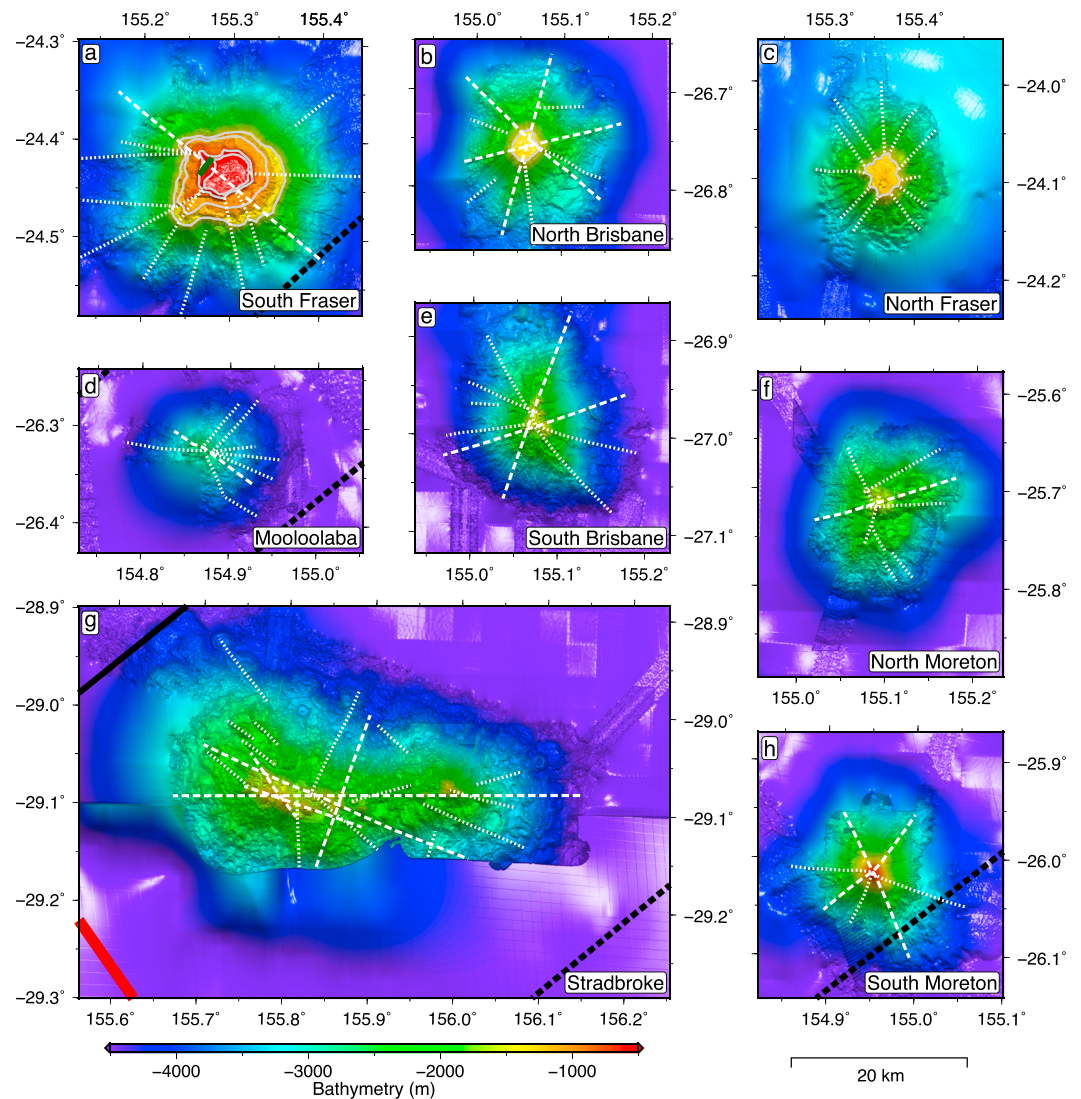
Figure 3. Bathymetry, structure, and tectonic setting of (a) South Fraser, (b) North Brisbane, (c) North Fraser, (d) Mooloolaba, (e) South Brisbane, (f) North Moreton, (g) Stradbroke, and (h) South Moreton. Extinct ridge segments and fracture zones as in Figure 1; other markings as in Figure 2. Scale is 1:400,000. Coordinate values given in meters are eastings and northings for Universal Transverse Mercator zone 56S. Larger maps can be found in Figures S2–S27.

Australia, using a LaCoste & Romberg gravimeter, yielding a drift correction of 2.8 mGal over 27 days. Eötvös corrections for changing speed and heading were applied, and the data filtered with an 800 s wide low-pass cosine filter, which yielded the optimal trade-off between signal-noise ratio and RMS crossover error. These data were used to calculate free-air (FAA) and Bouguer anomalies over the seamounts and to ground-truth regional satellite-derived gravity data from Sandwell and Smith (2009, V21.1) used in the flexure and gravity modeling.

Crossover analysis identified 547 internal crossovers with an average error of −0.1 and 7.3 mGal standard deviation. The median absolute deviation, which is less affected by outliers, is 5.5 mGal. Five crossovers include readings both before and after the urgent air-shock replacement at South Moreton Seamount, recording a mean error of 3.1 mGal, which is reasonable given the high gravity gradient (up to 0.15 mGal/m) in the area. Following this shutdown, the RMS deviation between satellite-derived and shipboard gravity data increased by 1.3 mGal, suggesting this repair may account for almost 50% of the total instrument drift.

The vertical gravity gradient data set of Sandwell et al. (2014) was used to map the extinct spreading center, with previous plate reconstructions, magnetic anomaly picks, and spreading symmetry (Gaina et al., 1998;

Hill, 1994), providing additional constraints in the northern Tasman Sea, where thick sedimentation and abundant volcanism complicates vertical gravity gradient interpretation. Magnetic anomaly data from the 1972 Bureau of Mineral Resources continental margin survey were used to locate the Continent-Ocean Boundary for modeling the gravity anomalies and seamount flexure (Gaina et al., 1998; Shaw, 1979).

2.3. Dredges

Thirty-five dredges and two Smith-McIntyre grab samples retrieved vesicular and nonvesicular mafic rocks, hyaloclastite, reef carbonate, and unlithified pelagic carbonate ooze (Cohen, 2012). This lithological information was used to tie morphological observations to geology and to constrain densities in gravity models.

3. Methodology

Here we analyze the geomorphological evidence of (1) volcanic growth, including volcanic rift zones, cones, and lava flows, and (2) erosion processes, such as headscars, narrow embayments, flat-topped summits, and hummocky debris, to understand the variations between seamounts and their relationship to underlying tectonic structures. Quantitative analysis of morphology, density, and lithospheric flexure is used to provide constraints on the relative impact of subplate, intralithospheric, and surface processes on the spatiotemporal evolution of the Tasmantid Seamounts.

3.1. Morphology Classification and Slope Analysis

We first qualitatively classify the seamounts based on key features such as terraces, a clearly defined summit, and the ruggedness of the flanks. We then use slope analysis to develop a quantitative framework for differentiating the groups. This analysis is also used to investigate the prevalence of submarine landslides across the chain, as mass transfer from over-steepened flanks to downslope regions should result in an overall decrease in slope gradient (Gee et al., 2001). Average slope gradient is calculated within 10° azimuthal bins from the seamount summit down to the deepest continuous closed contour around the base, with the exception of terraced seamounts. This category displays a bimodal slope distribution, with gentle gradients near the summits reflecting wave erosion and reef growth rather than a primary, constructional fabric (Figures 2 and 3). We thus split the slope analysis for these seamounts into calculations from the summit to the deepest terrace and from the deepest terrace to the base.

We then use manual three-dimensional analysis of the bathymetry to accurately delineate mass-wasting deposits and determine headscarp width/run-out distance ratios to determine mechanism, for example, slump, debris avalanche, or debris flow (Figure 4a). Maps of the slope gradient, the second derivative of the slope (Laplacian curvature), and multibeam backscatter are used to assess the overall roughness of the bathymetry and constrain the extent of potential mass-wasting deposits (Figures 4c and 4d). In addition to their uniform gradient, loose, rubbly mass-wasting deposits strongly diffract and attenuate incoming acoustic pulses, and therefore show up as regions of low reflectance backscatter as compared to flanks of in situ rock (Le Gonidec et al., 2003; Figure 4e).

3.2. Structural Orientations

To investigate if preexisting faults related to seafloor spreading may have impacted the morphology and structure of the Tasmantids, we map the orientations of the seamounts' volcanic ridges and elongation axes (Figures 2 and 3, Comment S2, and Figures S2–S27). We also determine the extinct ridge structure of the Tasman Sea (Comment S1 and Figure S1). We then group the seamounts according to tectonic setting (on fracture zone, on inside corner of ridge-transform intersections, etc.) and assess the consistency of trends to examine the importance of structural inheritance across the chain. Where seamounts span more than one category, we subdivide the mapped lineations according to local tectonic setting. For seamounts such as Mooloolaba or Stradbroke that span an entire short spreading segment, we divide the orientations into inside corner and outside corner domains for analysis, with no distinct midsegment stress regime due to the short segment length.

3.3. Gravity Reduction

Gravity anomalies across seamounts yield important insights into subsurface density structure, providing otherwise unobtainable information about volcanic evolution and intralithospheric processes (e.g., Paulatto et al., 2014). We calculate Bouguer anomalies by removing the gravitational effect of both sediment and volcanic basement topography from the FAA. The sedimentary cover is both thick and variable, often >1 km close to the continental margin. To account for this accurately, we combine OZ SEEBASE^{TM} (FROGTECH, 2014) sediment
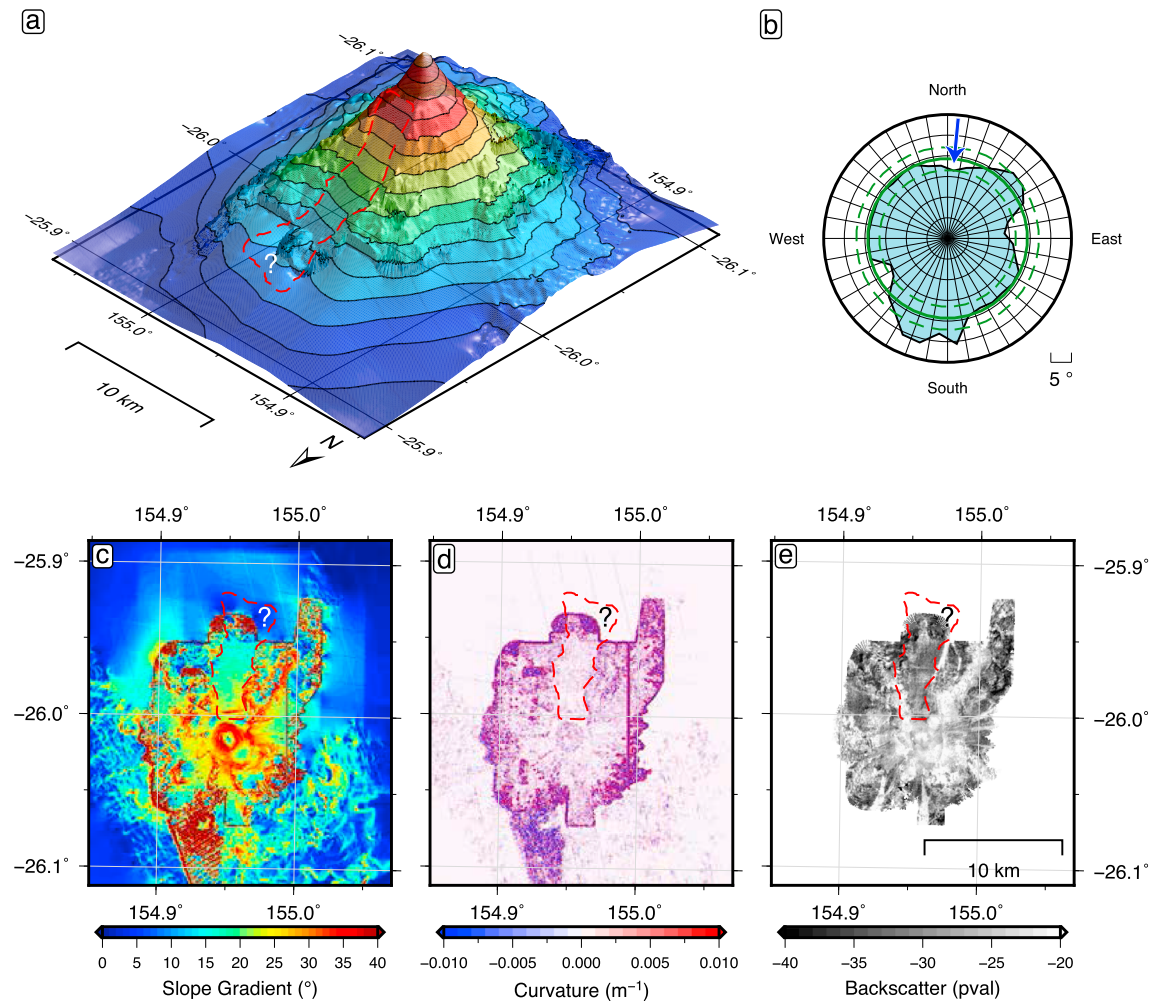
Figure 4. Slope analysis over conical South Moreton seamount. Mass wasting (red dashed line) on the northern flank is clearly visible in (a) 3-D bathymetry viewed from the northwest. (b) Mean slope gradient by sector. Blue arrow indicates mass-wasting event. Solid green line marks mean slope gradient across edifice; dashed green lines, the 1σ envelope. (c) Slope gradient, with the mass wasting having much smoother internal topography. (d) Laplacian curvature of bathymetry, again showing the mass-wasting deposit's smoother internal topography. (e) Backscatter, showing lower reflectivity within the mass-wasting deposit. Scale for (c)–(e) in bottom right corner of (e). The deposit extends beyond the high-resolution bathymetric data, so its full extent is unknown (indicated by question mark). The remainder of the slopes are dominated by rough topography due to lava flows and volcanic ridges.

thickness data, publicly available NGDC grids (Whittaker et al., 2013), and information on sediment thickness on seamount summits from the R/V *Southern Surveyor*'s TOPAS subbottom profiler to create a regional sediment thickness data set (Figure S28).

We then use Parker's equation to calculate the gravity anomaly across a density interface, Δg, in the wavenumber domain (Parker, 1973):

$$\Delta g(k_r) = 2\pi G(\rho_l - \rho_u)e^{-k_r d} \sum_{n=1}^{N} \frac{k_r^{n-1}}{n!} \mathfrak{F}\{h^n(x)\}, \tag{1}$$

where k_r is the radial wavenumber; G is the universal gravitational constant; ρ_l and ρ_u are the densities of the lower and upper layers, respectively; d is the mean depth of the interface; N is the order of the Taylor series describing the interface topography; $\mathfrak{F}$ is the forward Fourier transform; and $h(x)$ is the interface topography in the spatial domain (Parker, 1973). We use $N = 5$ to capture the gravity anomalies associated with rugged topography. We assume a water density of 1,030 kg/m³ and an average sediment density ($\bar{\rho}_s$) of 2,000 kg/m³, consistent with a sediment layer 1–2 km thick (Christensen & Stanley, 2003) and with values retrieved from process-oriented gravity modeling. The optimal basement density (ρ_c) is then determined by finding the value between 2,300 and 3,300 kg/m³ for which the coherence between bathymetry and Bouguer anomaly, weighted by spectral power, is minimized (Figure 5).
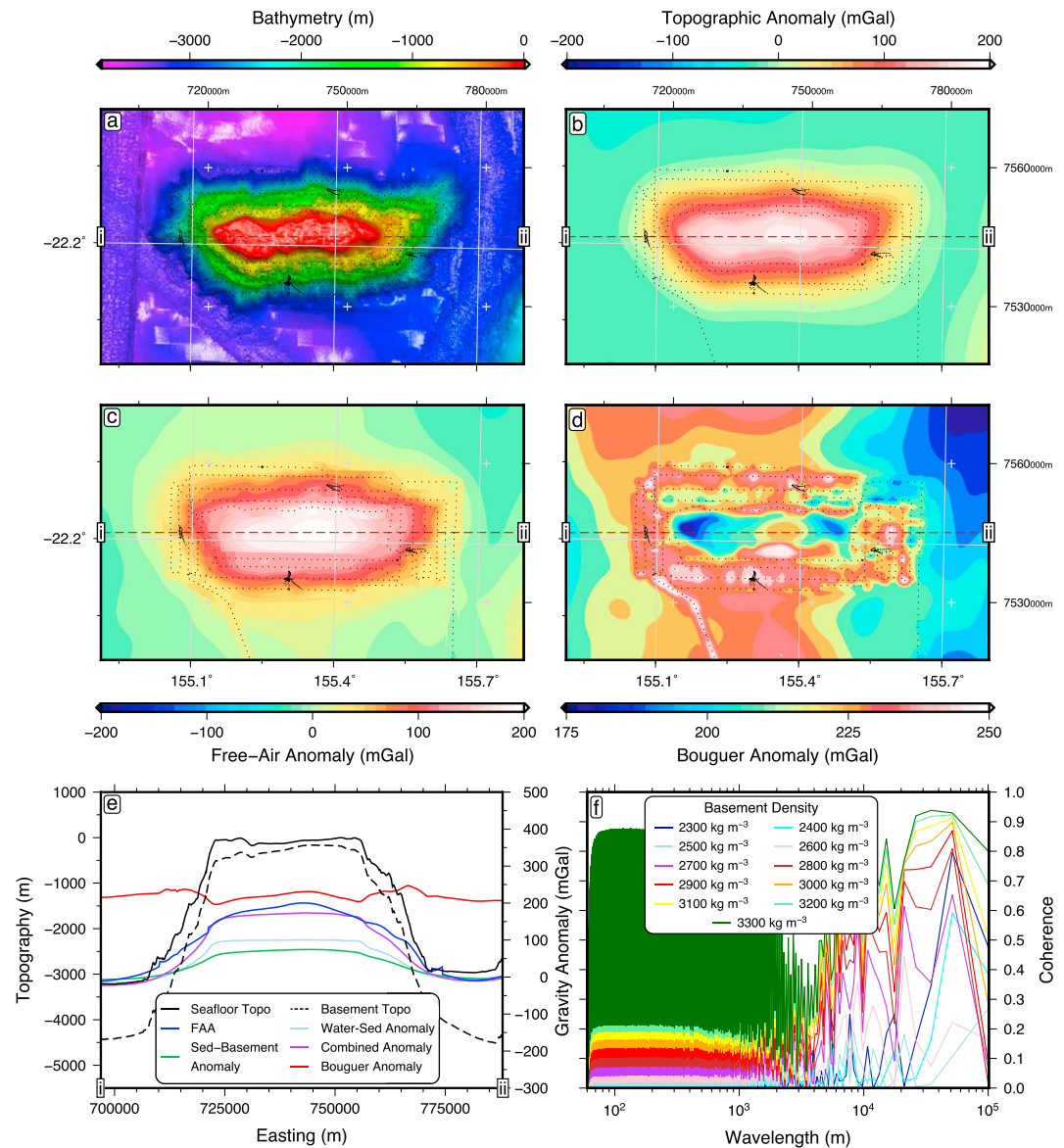
Figure 5. Bouguer gravity reduction over Wreck seamount. (a) Topography. (b) Topographic gravity anomaly from the water-sediment and sediment-basement interfaces, using ρ_c = 2,500 kg/m^3. (c) Free-air anomaly. (d) Resulting Bouguer gravity anomaly. (e) Topographic interfaces and gravity anomalies along Profile i–ii. (f) Coherence between gravity and topography for different ρ_c. The Bouguer reduction density is the ρ_c giving the lowest overall coherence after weighting by spectral power at corresponding wavenumber, 2,500 kg/m^3 in this case. FAA = free-air anomaly.

3.4. Elastic Thickness Analysis

The wavelength and amplitude of the flexure around major gravitational loads like seamounts reflect the long-term mechanical strength of the lithosphere. This can be approximated by the loading and deformation of an elastic plate of thickness T_e overlying an inviscid fluid (i.e., the asthenosphere; Watts, 1978). We use forward modeling to determine the T_e that best fits these flexural signatures in the bathymetry and gravity around each seamount. Seamounts south of Stradbroke that were not surveyed on TMD2012 are included in this analysis, which does not require high-resolution gravity or bathymetry data (Figure 1).

Thick sediment obscures flexural moats and bulges, so T_e cannot be determined directly from the bathymetry (Keene et al., 2008). Instead, we compare the observed FAA over each seamount with that predicted from prescribed 3-D load configurations and physical parameters. Due to the proximity of the continental margin, thick sediment partially burying the seamounts, and the seamounts' highly variable morphology, we define the volcanic load manually by tracing inflection points in the bathymetry's directional derivative. 2-D
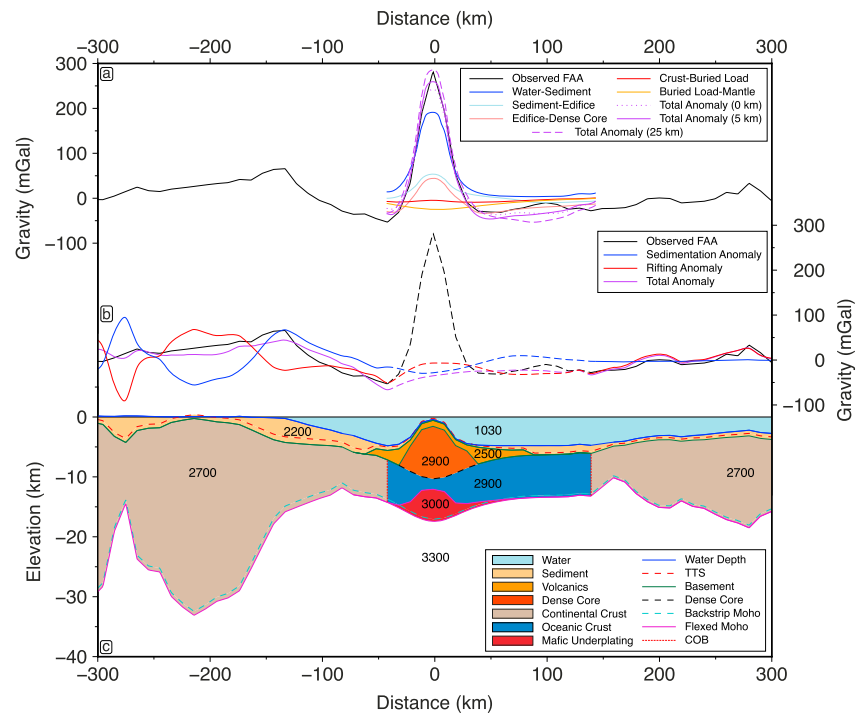
Figure 6. Gravity modeling over Queensland Guyot showing load geometries and densities (kg/m^3), together with observed and calculated FAAs. (a) Calculated gravity anomalies for each density interface across Queensland Guyot (T_e = 5 km). Total anomalies also shown for T_e = 0 km and T_e = 25 km. Profiles are cut at the continent-ocean boundary. (b) Process-oriented gravity modeling across the east Australian margin. Queensland Guyot is excluded from this analysis (see dashed lines). (c) Load geometry along transect. TTS = total tectonic subsidence; COB = continent-ocean boundary; FAA = free-air anomaly. Observed free-air gravity anomaly combines shipboard gravity data across the seamount with satellite-derived data from Sandwell and Smith (2009, V21.1).

process-oriented gravity modeling (e.g., Watts, 1988) is used to explicitly include both sediment and seamount loading (Figure 6), including testing both constant and thickness-dependent sediment densities using the compaction length and initial porosity parameters of Czarnota et al. (2013).

We then test a range of 3-D models incorporating flexural responses to both seamount and sedimentary loads with the complexity of the seamount ranging from models of a simple volcanic edifice with a single density to models that include dense intrusive cores and/or intracrustal intrusions (Contreras-Reyes et al., 2010; Kim & Wessel, 2010). Because the sedimentation history is quite uncertain, we also test the sensitivity of our results to a significant error in sediment thickness or the T_e associated with the sediment. A full description of all models tested is given in Comment S3. For each model, the RMS misfit between observed and modeled gravity anomalies is used to estimate a best-fitting T_e, with 125% of the minimum misfit used to estimate upper and lower bounds (e.g., Kalnins & Watts, 2009; Watts et al., 2006).

To capture the range of T_e estimates associated with different forward models, we calculate the minimum, maximum, mean, median, and interquartile range for each seamount as well as the model yielding the lowest misfit at each seamount. These calculations exclude model results that do not yield a constrained misfit minimum within the tested range (0 km $\leq T_e \leq$ 50 km).

4. Results

4.1. Morphology Classification

Although the Tasmantids' morphology is highly variable, we qualitatively divide the seamounts into four categories: (1) large, elongated guyots with multiple terraces; (2) rugged seamounts with numerous, cross-cutting volcanic rift zones; (3) conical seamounts resembling submarine stratovolcanoes with summit vents and isolated flank cones; and (4) low gradient shield seamounts surrounded by fields of volcanic cones.

Of the 14 volcanic edifices investigated during TMD2012, terraced seamounts are the most numerous, comprising seven edifices: Wreck, North Recorder, South Recorder, Queensland, North Britannia, Central Britannia,

and South Britannia (Figures 2a, 2c, and 2d). Dredge samples indicate that the lower slopes (>1,500 m depth) are largely mafic lavas and volcanic breccias, while the upper slopes and terraces include vesicular and nonvesicular mafic rocks, hyaloclastite, volcaniclastic sandstone, and reef carbonate. The reef material and consistent elevation of the terraces confirms that they are reef or wave-cut terraces, rather than primary volcanic features such as lava deltas (e.g., Chaytor et al., 2007). Large, deep arcuate indentations on some upper terraces (e.g., Central and South Britannia) suggest substantial mass-wasting events, while lower slopes are dominated by much smaller headscarps.

The larger terraced seamounts like Britannia and Queensland typically have three to five terrace levels with depths of 300–1,450 m, far exceeding Cenozoic glacioeustatic variations. For example, 1,450 m of cumulative subsidence must have occurred at Queensland since the formation of the lowest terrace, with continued cooling of the underlying oceanic crust accounting for 610 m. Several factors may contribute to the residual 840 m of subsidence: (1) flexure due to the neighboring Britannia seamounts (e.g., Huppert et al., 2015); (2) continued northward motion off the plume swell; (3) regional sedimentation; or (4) dynamic topography (e.g., Czarnota et al., 2014; DiCaprio et al., 2010).

There are four seamounts with conical morphology: North Fraser, South Fraser, North Brisbane, and South Moreton (Figures 3a, 3b, 3c, and 3h). Dredging recovered predominantly vesiculated basalt and hyaloclastite, together with significant quantities of reef carbonate near the summits. North Fraser, South Fraser, and North Brisbane have small wave-cut terraces and summits, indicating exposure above wave-base. These beveled surfaces are covered with hummocky, carbonate-rich reef deposits. Wide headscarps and characteristically smooth slopes indicate moderate- to large-scale mass wasting. Although rare, there are some mass-wasting deposits with a high ratio of run-out distance to headscarp width, indicating debris avalanches (Figure 4).

Four seamounts have rugged morphology: Mooloolaba, North Moreton, South Brisbane, and Stradbroke (Figures 3d to 3g). These are composed of a dense network of intersecting volcanic ridges and vents and do not have a single, clear summit. They have no terraces and little or no unequivocal evidence of mass wasting. Dredging recovered a mix of hyaloclastite, vesicular, and nonvesicular basalt. North Moreton and Stradbroke also yielded volcaniclastic-rich carbonate rocks, suggesting some reworking near sea level, although the conspicuous lack of planation surfaces suggests at most limited exposure above wave-base. If the typical water depth, and therefore confining pressure, were systematically different for rugged and conical seamounts then associated changes in volcanic explosivity might explain their contrasting morphologies (Kokelaar, 1986). However, as both rugged and conical seamounts have upper sections demonstrably erupted near sea level, this suggests that deep structure is behind their fundamental difference in morphology.

The only shield seamount identified, Cato, sits atop the Lord Howe Rise (Figure 2b), and has a broad, low-angled base topped by a modern coral reef. Its most distinctive feature is the numerous (>75) parasitic volcanic cones, typically 250 m high and 1.5 km wide. Dredging one cone recovered altered scoriaceous material, indicating relatively explosive eruption in a subaerial or shallow marine environment. The continental crust underlying Cato may contribute to the diffuse volcanism by creating more complex magmatic plumbing, spreading the magmatism over a wider area. As with the terraced seamounts, some large arcuate indentations on the upper slopes indicate significant mass-wasting events.

Slope gradient analysis shows quantitative differences between these qualitative morphological categories. The lower slopes of the terraced seamounts have an intermediate mean gradient (17.4°) with very low intersector variability ($1\sigma = 1.3°$), suggesting this is a naturally stable slope angle in what is likely relatively unconsolidated material. The upper slopes have a low mean gradient (9.7°) and intermediate intersector variability ($1\sigma = 2.1°$; Figures 7a.i and 7a.ii), due to wave erosion and reef growth reducing the average gradient and larger scale mass wasting increasing intersector variability. The compact conical edifices typically steepen toward the summit and have a high mean gradient (18.1°) and intermediate intersector variability ($1\sigma = 2.5°$). In contrast, rugged seamounts generally exhibit a lower (but still moderately high) mean gradient (17.0°) but higher intersector variability ($1\sigma = 3.1°$), reflecting their diffuse, fissure-fed volcanism and multiple peaks (Figures 7b and 7c). The shield seamount, Cato, has a very low gradient (6.8°), consistent with subaerial or shallow marine eruption, as suggested by dredging results, and relatively high intersector variability ($1\sigma = 2.9°$; Figure 7d), again reflecting diffuse volcanism. The morphology of Cato and Wreck is also influenced by their continued presence at sea level, with active wave action and reef growth.
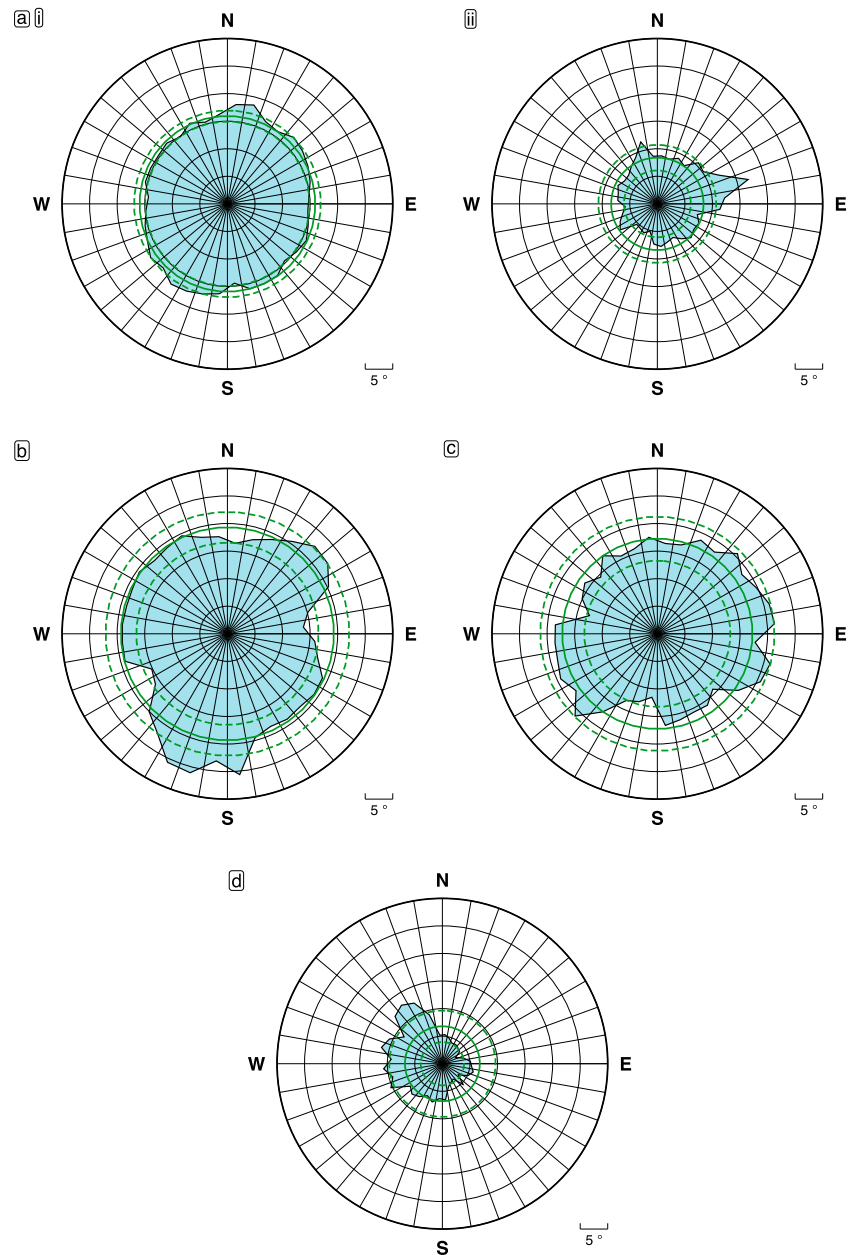
Figure 7. Examples of mean slope gradient by sector, showing the distinctive characteristics of each category. (a) Terraced Britannia: (i) basal and (ii) upper, subaerially eroded slopes. (b) Conical South Moreton. (c) Rugged Stradbroke. (d) Shield Cato. Solid green lines mark the mean slope gradient; dashed green lines, the 1σ envelope.

Large mass-wasting deposits are not as common on the Tasmantids as on other major seamount chains (e.g., Fornari et al., 1979; Moore et al., 1989; Mitchell et al., 2002), although smaller-scale events are widespread. None of the seamounts show signs of major sector failures, which is unusual given their size and age (Wessel et al., 2010). The generally high slope gradients across the chain coupled with modest rates of mass wasting point to volcanism with a high intrusive to extrusive ratio (Ramalho et al., 2013).

4.2. Structural Orientations and Correlation With Ridge Structure

A striking feature of the Tasmantids is the inconsistent orientation of the edifices and volcanic ridges (Figures 1–3), in contrast to chains such as Hawaii-Emperor and Louisville, which are generally elongated parallel to absolute plate motion (Koppers et al., 2012; Tarduno et al., 2003; Wessel, 1993) and the subparallel elongate ridges associated with intraplate extension such as Pukapuka Ridge, Crossgrain Ridge, and the Musician Seamounts (Lynch, 1999; O'Connor et al., 2015; Sandwell et al., 1995). In fact, some Tasmantid Seamounts
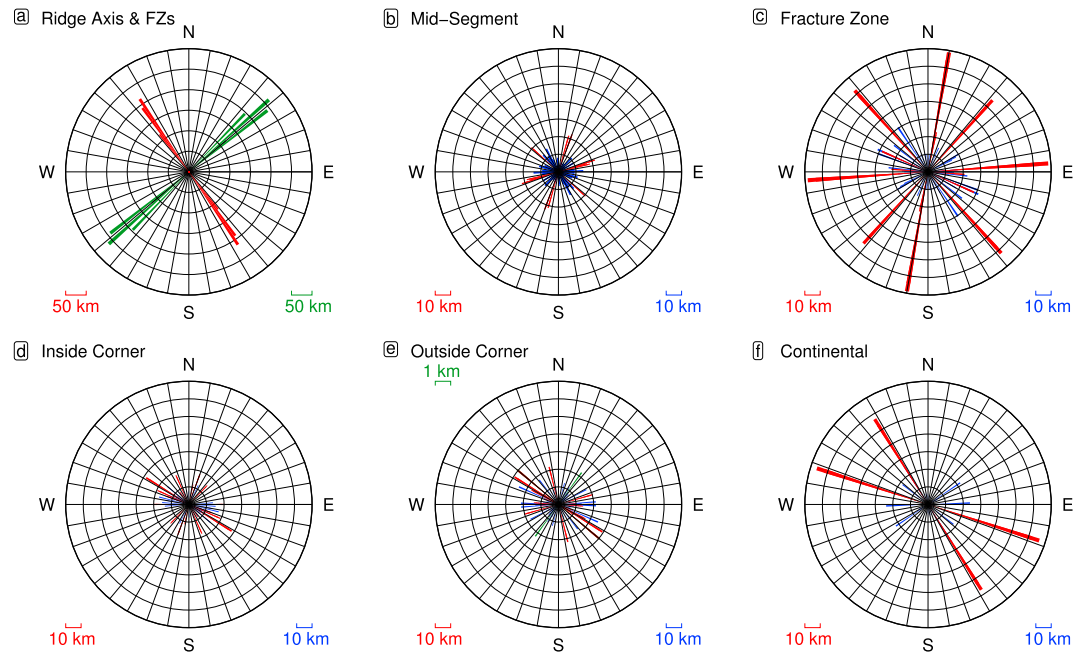
Figure 8. Structural orientations by tectonic setting. (a) Ridge segments (red) and fracture zones (green). (b) Volcanic ridge orientations (blue), principal axes of elongation (red), and faults (green) for seamounts emplaced midsegment (North Fraser, North Moreton, North Brisbane, and South Brisbane); (c) across fracture zones (Wreck, South Recorder, Queensland, northern Central Britannia, and southern South Britannia); (d) at inside corners of ridge-fracture zone intersections (South Moreton, southern Mooloolaba, southern North Britannia, northern South Britannia, and western Stradbroke); (e) at outside corners (South Fraser, North Recorder, northern Mooloolaba, northern North Britannia, southern Central Britannia, and eastern Stradbroke); and (f) on crust of unequivocally continental nature (Cato). Edifice construction is clearly influenced by preexisting structures inherited from Tasman seafloor spreading.

are oriented perpendicular to the predominantly northward absolute motion of the Australian plate, for example, Wreck and Stradbroke (Figures 2a and 3g). However, the Tasmantid Seamounts are emplaced over pre-existing Tasman Sea spreading structures whose axial segments trend NNW-SSE and whose fracture zones and transforms strike WSW-ENE (Figure 8a). A spreading-related influence similar to that of active spreading centers (Dick et al., 2003; Hekinian et al., 1999) might thus explain the Tasmantids' diverse orientations.

Analysis of the structural orientations confirms similar patterns among seamounts in similar tectonic settings. At midsegment seamounts like North Brisbane, the lineations are generally short and show a stellate pattern with no clear relationship with the spreading ridge structure (Figures 8a and 8b, diagrams for individual edifices in Figures S29–S31). Seamounts emplaced along fracture zones, such as North Recorder, often have dominant trends subparallel to either the fracture zone or the spreading ridge, with minor ridges predominantly subparallel to the ridge axis. Both major and minor trends are often rotated anticlockwise to the spreading geometry, perhaps reflecting magma exploiting spreading-related extensional faults coupled with transform-induced fault rotation (Figure 8c). Trends at inside corner seamounts such as North Britannia are varied, but are longest and most numerous in the sector between the ridge and the E-W axis, showing a similar anticlockwise rotation to seamounts at fracture zones. Structural orientations for seamounts emplaced at outside corners are highly varied, with the limited evidence of preferred orientations suggesting a similar pattern as for inside corner seamounts (Figure 8e). Across fracture zone, inside corner, and outside corner settings, the trends of seamounts emplaced on very short spreading segments seem to show greater rotation than those of seamounts emplaced on longer spreading segments, consistent with the rotation arising from the interaction between extensional and transform motion. Trends at Cato are predominantly ridge-oblique, potentially indicating fault trends related to Mesozoic rifting of the Lord Howe Rise (Figure 8f).

Orientation analysis thus suggests that extinct ridge structure significantly influences magmatic conduit orientation, even >20 Ma after spreading ceased. Elongate seamounts predominantly occur on fracture zones or inside corners and tend to be both large and tall, with extensive wave-cut platforms and multiple terraces (Table 1). The terraces obscure the original morphology, so we cannot distinguish between rugged and

Table 1
Morphological, Structural, and T_e Results Along the Chain From Oldest (Northernmost) to Youngest (Southernmost)

Seamount	Morph. class	Footprint shape	Structural setting	Red. density (kg/m³)	Age diff. (Ma)	T_e Range (km)	Median T_e (km)	Mean T_e (km)	best Model T_e (km)
Wreck	Terraced	Elongate	Continent or spans fracture zones[a]	$2,520^{+60}_{-65}$	25.8 ± 2.9[b]	0–4	0^{+1}_{-0}	0^{+1}_{-0}	0^{+1}_{-0}
Cato	Shield	Circular	Continent	$2,115^{+90}_{-110}$	N/A	0–5	0^{+2}_{-0}	0^{+2}_{-0}	1^{+1}_{-1}
North Fraser	Conical	Circular	Midsegment	$2,655^{+535}_{-655}$	25.5 ± 1.7[c]	2–7	2^{+2}_{-1}	3^{+3}_{-1}	2^{+2}_{-1}
South Fraser	Conical	Circular	Outside corner	$2,725^{+100}_{-115}$	24.3 ± 1.4[c]	1–10	5^{+1}_{-1}	5^{+2}_{-1}	2^{+2}_{-2}
North Recorder	Terraced	Semi-elongate	Outside corner	$2,765^{+65}_{-65}$	25.4 ± 1.1[c]	5–9	$6^{+1.5}_{-1}$	7^{+2}_{-1}	8^{+3}_{-2}
South Recorder	Terraced	Elongate	Fracture zone	$2,780^{+70}_{-110}$	27.0 ± 1.0	0–5	2^{+0}_{-1}	2^{+1}_{-1}	1^{+1}_{-1}
North Moreton	Rugged	Circular	Midsegment	$2,870^{+190}_{-200}$	29.0 ± 0.8[c]	0–24	0^{+6}_{-0}	4^{+5}_{-2}	0^{+4}_{-0}
South Moreton	Conical	Circular	Inside corner	$2,965^{+65}_{-70}$	29.8 ± 0.8[c]	0–22	$10.5^{+4}_{-4.5}$	10^{+6}_{-4}	12^{+6}_{-3}
Mooloolaba	Rugged	Circular?	Spans inside to outside corner[a]	$2,305^{+360}_{-305}$	29.6 ± 0.8[c]	0–25	$1^{+3.5}_{-1}$	6^{+8}_{-2}	0^{+2}_{-0}
North Brisbane	Conical	Circular	Midsegment	$2,910^{+80}_{-95}$	31.6 ± 0.9	2–5	4^{+2}_{-2}	4^{+2}_{-2}	5^{+1}_{-2}
South Brisbane	Rugged	Semi-elongate	Midsegment	$2,815^{+100}_{-130}$	32.4 ± 1.0[c]	1–7	6^{+2}_{-3}	5^{+2}_{-3}	5^{+2}_{-2}
Queensland	Terraced	Semi-elongate	Fracture zone	$2,800^{+65}_{-35}$	34.7 ± 1.6[c]	2–6	$4^{+1}_{-0.5}$	4^{+1}_{-1}	$4^{+1}_{-0.5}$
North Britannia	Terraced	Elongate	Spans inside to outside corner[a]	$2,710^{+90}_{-110}$	33.5 ± 1.8	0–14	8^{+2}_{-2}	6^{+7}_{-2}	14^{+2}_{-3}
Central Britannia	Terraced	Elongate	Outside corner/fracture zone	$2,685^{+45}_{-35}$	32.7 ± 1.5	0–13	1^{+1}_{-1}	2^{+2}_{-3}	2^{+0}_{-2}
South Britannia	Terraced	Elongate	Inside corner/fracture zone	$2,620^{+70}_{-50}$	33.1 ± 1.3	0–11	1^{+1}_{-1}	2^{+1}_{-1}	1^{+1}_{-1}
Stradbroke	Rugged	Elongate	Spans inside to outside corner[a]	$2,855^{+150}_{-155}$	36.1 ± 1.0	0–39	$0.5^{+2.5}_{-0.5}$	11^{+6}_{-4}	0^{+2}_{-0}
Unnamed	—	—	Outside corner		39.8 ± 1.3[c]	4–7	6^{+1}_{-1}	6^{+1}_{-1}	7^{+1}_{-1}
Derwent Hunter	—	—	Spans three fracture zones[a]		46.5 ± 1.2	2–8	$5^{+1}_{-0.5}$	5^{+2}_{-1}	7^{+2}_{-1}
Barcoo-Taupo[d]	—	—	Spans inside corner to inside corner[a]		54.0 ± 0.6	0–8	$6.5^{+2}_{-1.5}$	6^{+2}_{-2}	8^{+2}_{-1}
Kimbla	—	—	Midsegment		50.0 ± 0.1[c]	0–2	2^{+1}_{-2}	2^{+1}_{-2}	2^{+1}_{-2}
Gascoyne	—	—	Outside corner/fracture zone		52.3 ± 1.2	0–2	$0.5^{+1.5}_{-0.5}$	1^{+1}_{-1}	0^{+1}_{-0}

Note. Age differential uses seamount ages from Kalnins et al. (2015) and seafloor ages from Müller et al. (2008). For best model T_e, where the minimum RMS misfit for a seamount is shared by multiple models, the T_e estimate and uncertainties also match, with the exception of the lower bound for Queensland, where an average has been used. Seamounts from Unnamed south have incomplete or no multibeam bathymetry and therefore do not have morphology classifications or reduction densities. [a]Due to short spreading segments, these seamounts span three or more settings. [b]Only applicable if Wreck is emplaced on oceanic lithosphere. [c]No ^{40}Ar-^{39}Ar age for seamount, ages and errors estimated by linear interpolation between dated locations. [d]Guyots not subdivided due to lack of high-resolution data.
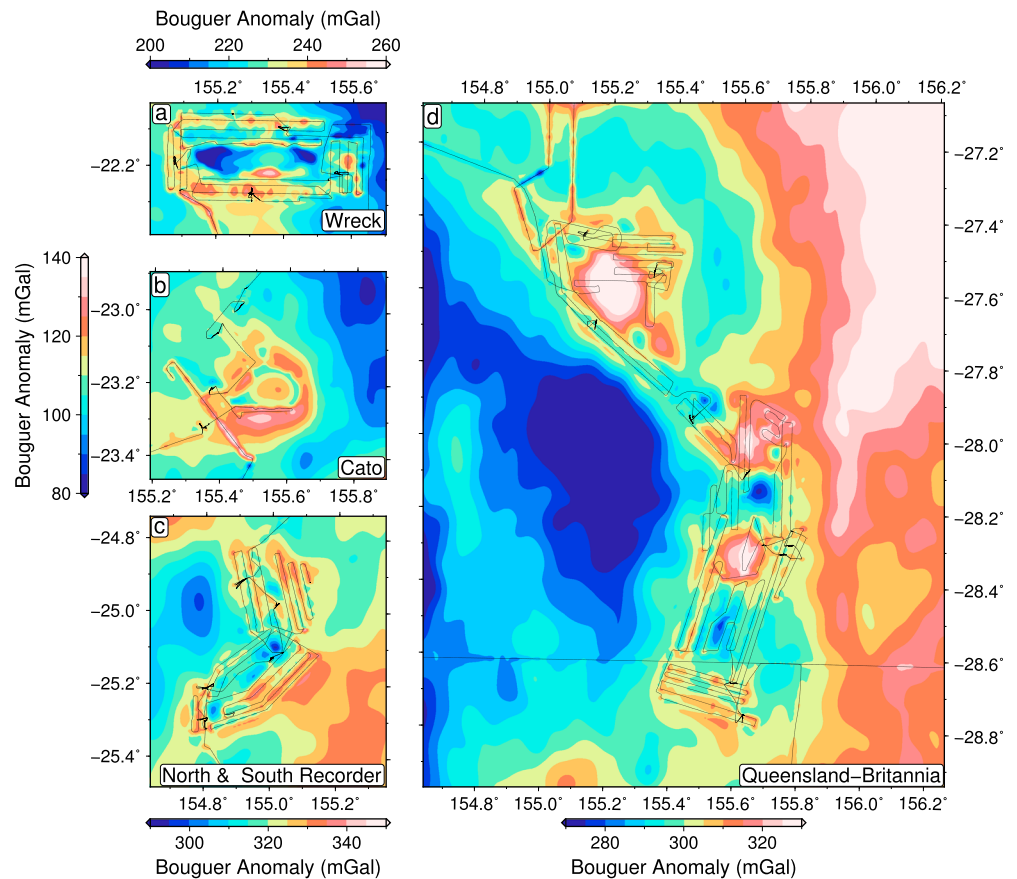
Figure 9. Bouguer anomalies over (a) Wreck, (b) Cato, (c) North and South Recorder, (d) Queensland and the Britannias. Black dots mark the shipboard gravity path. Residual highs of 30–60 mGal over many edifices (e.g., Central Britannia and Queensland) indicate substantial intrusive cores significantly denser than the reduction density. For continuity, (c) and (d) use reduction densities for the whole area shown, 2,760 and 2,690 kg/m³, respectively. Each color scale spans 60 mGal. Coordinate values given in meters are eastings and northings for Universal Transverse Mercator zone 56S. Larger maps for the individual edifices are shown in Figures S32–S47.

conical underlying constructional styles. Seamounts located midsegment or at outside corners tend to have a circular footprint and are more likely to be conical, although South Moreton, located on an inside corner, is also circular and conical. Rugged seamounts are observed in every setting except directly on a fracture zone.

4.3. Gravity Reduction and Deep Volcanic Structure

Bouguer reduction densities for most of the seamounts range from 2,620 to 2,965 kg/m³ (Table 1), suggesting a relatively high proportion of intrusive volcanism or massive basalt flows, with smaller contributions from hyaloclastite and rubbly or porous surface eruptions. At the upper end of this range, the densities are similar to those for pristine gabbro, suggesting relatively thin veneers of basalt and hyaloclastite over large intrusive cores, similar to that proposed by Contreras-Reyes et al. (2010) for Louisville Guyot. About half the edifices are also underlain by large magnitude (up to 50 mGal), subcircular Bouguer anomaly highs, indicating a mass excess and again suggesting the presence of dense (>2,800 kg/m³) intrusive cores (Figures 9 and 10). This is particularly common in seamounts with comparatively low reduction densities, for example, North and Central Britannia (Figure 9d), making a high density component very widespread along the chain.

In contrast, Wreck, Cato, and Mooloolaba have lower reduction densities of 2,520, 2,115, and 2,305 kg/m³, respectively. For Cato, the residual Bouguer highs associated with the limited ship-based gravity collected (due to poor weather) suggest 2,115 kg/m³ is likely an underestimate, with lower frequency satellite-based measurements not capturing the full anomaly, although this probably cannot explain the full reduction relative to the majority of the chain. Mooloolaba's reduction density is also poorly constrained due to the combination of comparatively low relief and incomplete multibeam coverage; its range of 2,000–2,665 kg/m³ overlaps with the densities of the other seamounts. A genuinely lower density, as is likely at least at Cato and
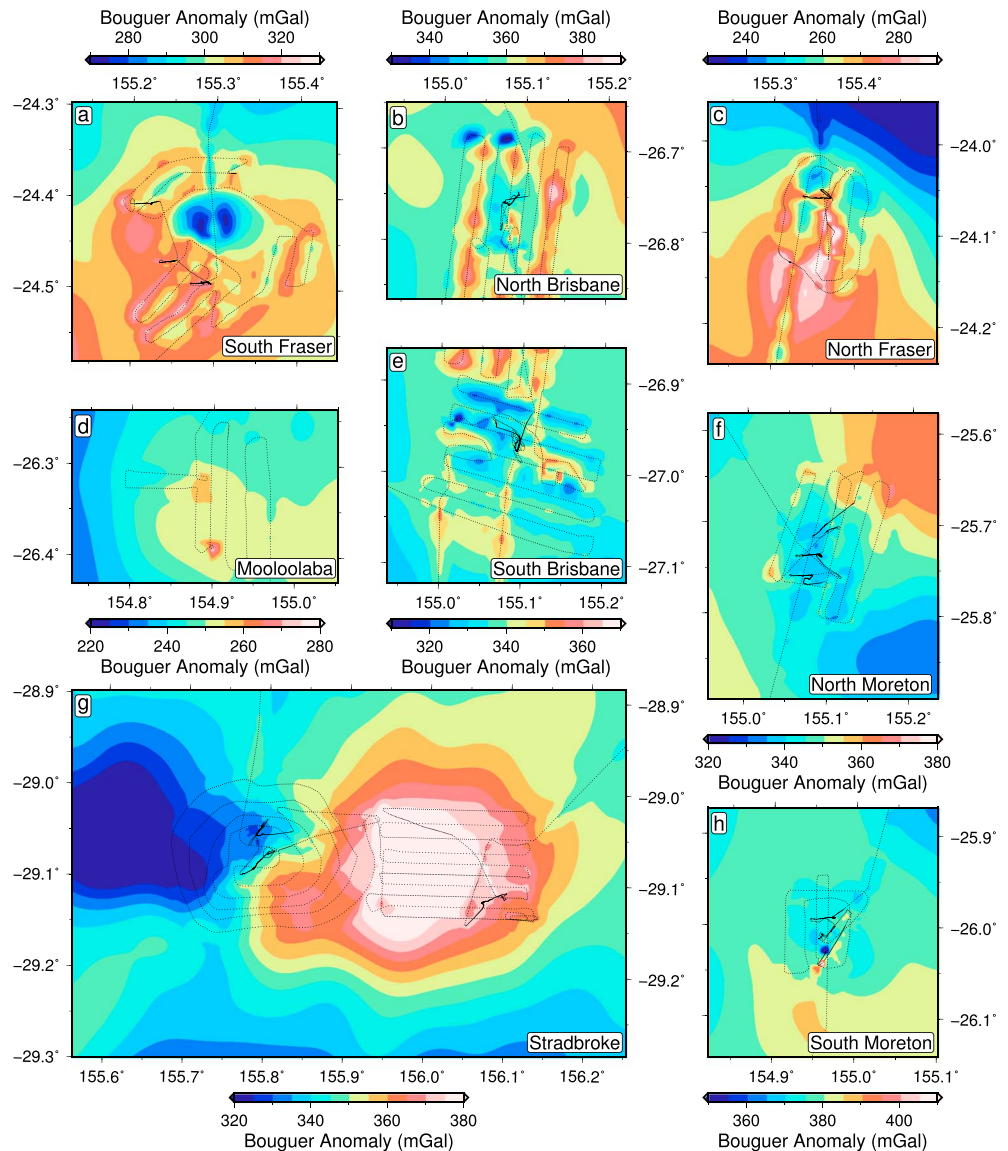
Figure 10. Bouguer anomalies over (a) South Fraser, (b) North Brisbane, (c) North Fraser, (d) Mooloolaba, (e) South Brisbane, (f) North Moreton, (g) Stradbroke, and (h) South Moreton. Black dots mark the shipboard gravity path. Each color scale spans 60 mGal. Coordinate values given in meters are eastings and northings for Universal Transverse Mercator zone 56S. Larger maps for the individual edifices are shown in Figures S32–S47.

Wreck, could indicate either a higher proportion of loosely consolidated rocks, such as hyaloclastite or later carbonate, or a change in magma composition.

4.4. Strength of the Underlying Lithosphere

Using a combination of 2-D process-oriented and 3-D forward modeling, we find that mean T_e varies between 0 and 11 km along the chain, with large differences between adjacent edifices and no obvious trend (Tables 1 and S1). Although the best-fitting model varies between seamounts, configurations incorporating a large, dense intrusive core (2,900 kg/m^3) covered with a thin, 2,500 kg/m^3 layer with or without magmatic underplating give consistently lower misfits than either the reference model or models with just underplating (Figures S48–S49 and Table S1). This is consistent with the prevalence of high densities and residual Bouguer anomaly highs across the chain, but misfit generally increases for models with an even higher density edifice (3,000 kg/m^3 core and 2,600 kg/m^3 carapace).

Process-oriented gravity modeling that includes flexure driven by both the seamounts and the thick sediment cover (~1 km) was used to constrain the density and T_e associated with the sediments. This yields a best-fitting
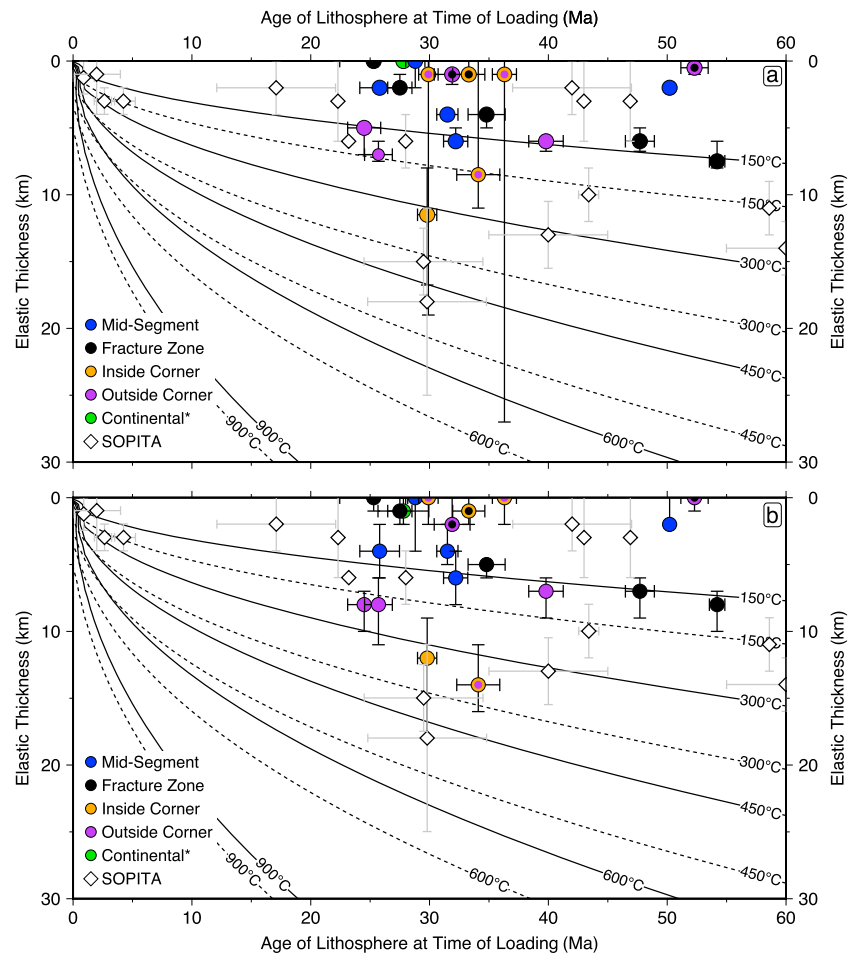
Figure 11. T_e versus age of lithosphere at time of loading, using seamount ages from Kalnins et al. (2015) and seafloor ages from Müller et al. (2008). (a) median T_e and interquartile range for each seamount across all models. Symbol size scales with number of well-constrained models. Seamount data from the SOPITA are shown for comparison, collated from Calmant and Cazenave (1987), Smith et al. (1989), Goodwillie and Watts (1993), Maia and Arkani-Hamed (2002), and Lee et al. (2009). (b) T_e and associated uncertainty for best-fitting model at each seamount. Symbol size indicates scales with number of well-constrained models. Uncertainty in differential age is not shown if error bars would be smaller than symbol size and predicted isotherms are from the plate cooling models of Turcotte and Schubert (2002; solid) and McKenzie et al., (2005; dashed). Virtually all seamounts plot significantly shallower than the 300–600° C range for normally maturing oceanic lithosphere. *Notional differential age used for Cato, emplaced on continental lithosphere, to allow plotting. SOPITA = South Pacific Isotopic and Thermal Anomaly.

$\bar{\rho}_s$ of ~2,000 kg/m^3, identical to the value used for the Bouguer anomaly. The mean best-fitting T_e associated with sediment loading ($T_{e\,sediment}$) is 17 km, irrespective of whether lateral variation in $\bar{\rho}_s$ is included. There is some indication of lower $T_{e\,sediment}$ values in the north, consistent with the younger lithosphere there, but high variability suggests local differences in sedimentation history may also strongly influence the observed $T_{e\,sediment}$. Although including the substantial sediment load is essential for model stability, the estimates of T_e for the seamounts are largely insensitive to the specifics of the sediment. Dense core models using a $T_{e\,sediment}$ of 0 or 34 km or increasing or decreasing the sediment thickness by 50% throughout the basin typically yielded T_e estimates within 1–2 km of those from the reference dense core model (Table S1). In most cases, a higher sediment density of 2,200 kg/m^3 has a similar effect on seamount T_e, although a few seamounts (North Recorder, North Moreton, Mooloolaba) yield anomalously high T_e estimates for some models with this sediment density (Table S1). Overall, our seamount T_e estimates should not be significantly affected by uncertainties associated with the poorly constrained sediment load.

Oceanic T_e is normally expected to increase with lithospheric age at the time of loading (i.e., $t_{crust} - t_{load}$), correlating with the depth to the 300–600° C isotherms (e.g., Watts, 1978; Watts & Zhong, 2000). However, most

seamounts plot near or above the 150° C isotherm, corresponding to a much weaker than normal lithosphere (Figure 11). With such a shallow isotherm, it is difficult to distinguish a relationship between age differential and T_e. The data do suggest a slight variation in T_e with tectonic setting. Seamounts in fracture zone, midsegment, and rifted continental settings consistently show very low T_e. Seamounts on inside and outside corners show a wide range of values, but generally account for the highest T_e estimates along the chain.

5. Discussion

Except for Wreck, Cato, and Mooloolaba, the Tasmantids' Bouguer reduction densities (2,620–2,965 kg/m^3) are higher than the ~2,400–2,600 kg/m^3 values estimated from seamounts studied by Le Pichon and Talwani (1964), Jilinski et al. (2013), and Paulatto et al. (2014) and are in the upper half of the distribution for the western Pacific from Kalnins and Watts (2009), which had a median of 2,600 kg/m^3. They are comparable to values estimated for the Hawaiian Islands by Watts et al. (2006) and for Louisville Guyot by Contreras-Reyes et al. (2010). These higher densities are partly explained by our explicit removal of sediment before calculating seamount density, as well as by the dense cores. Although not widespread, such intrusive cores have been found at Louisville (Contreras-Reyes et al., 2010), Great Meteor (Weigel & Grevemeyer, 1999), and La Réunion (Gallart et al., 1999) and inferred from uplift histories in Cape Verde (Ramalho et al., 2010) and Madeira (Ramalho et al., 2015). The residual Bouguer highs that persist despite the high reduction densities suggest possible ultramafic bodies in the lower crust, a potentially interesting intermediate case (20–50 Ma at emplacement) for the model of Richards et al. (2013), which suggests this is characteristic of intraplate volcanism emplaced on thick, mature oceanic lithosphere, where initial melting is deep, such as the deep crustal intrusions of El Hierro (Klügel et al., 2015).

This gravity evidence combined with slope analysis showing low rates of mass wasting demonstrates that Tasmantid Seamounts have high intrusive to extrusive ratios. The high proportion of intrusive volcanic growth, coupled with the strong dependence of morphology on preexisting ridge structure, points to sluggish magma extraction and a relatively weak temperature anomaly in the underlying mantle. This is further supported by a maximum of ~840 m residual subsidence identified from the terraced seamounts, significantly less than the positive ~1,000–2,000 m residual depth anomalies observed over the Iceland and Hawaiian plumes (e.g., Winterbourne et al., 2014), particularly once other sources of subsidence such as the heavy sedimentation and regional dynamic topography (e.g., Czarnota et al., 2014; DiCaprio et al., 2010) are included.

In contrast, Cato, Wreck, and Mooloolaba are characterized by Bouguer reduction densities <2,600 kg/m^3. Lower densities could be ascribed to higher proportions of unconsolidated rock or carbonate. Modern coral reefs do cap Cato and Wreck, but at least several hundred meters of reef would be needed to significantly decrease the overall reduction density. While this is possible, most of the terraced seamounts with high reduction densities also have carbonate material and reef morphology, making it less likely that reef growth alone explains the decrease.

Alternatively, Cato is emplaced on thinned continental crust; contamination of mafic magma and the evolution of more felsic compositions through increased residence time could reduce the density. Wreck is located in the Cato Trough, a region of ~3,000 m deep water whose crustal nature is not well established. Although the reconstructions of Gaina et al. (1998) suggest it could be incipient oceanic crust, they identify no marine magnetic anomalies in the basin. Exon et al. (2006) consider that the area could be highly extended continental crust. It is thus possible that Wreck is also emplaced on continental basement. In this scenario, the contrast in morphological style between the shield of Cato and the elongated, terraced Wreck could be attributed to melt focusing along a substantial fault or to thinner crust underlying Wreck, facilitating faster rates of magma generation and extraction with less intracrustal storage and crystal fractionation. However, further work on the nature of the crust and margins in this region is required. If Cato Trough proves to be underlain by continental crust, the recent redefinition of the Lord Howe Rise, Challenger Plateau, and New Zealand as a separate continent, Zealandia, would need to be reevaluated according to the definition of Mortimer et al. (2017). Neither underlying continental basement nor extensive reef deposits plausibly explains rugged Mooloolaba's low density, but this value is poorly constrained.

The Tasmantids' unusual diversity of location and orientation relative to absolute plate motion, footprint shape, and overall morphology can be correlated with the seamounts' emplacement over the extinct
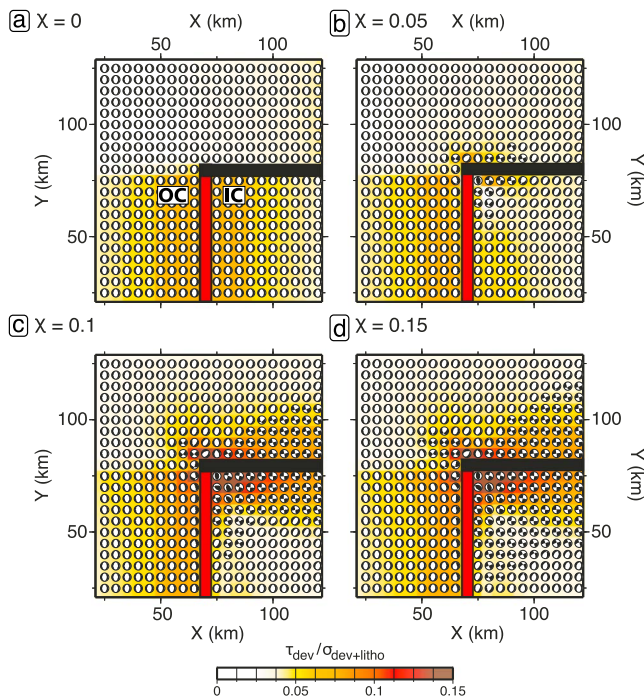
Figure 12. Influence of mechanical coupling across transforms on stress orientations (after Behn et al., 2002). Focal mechanisms show optimal fault planes, with color shading showing the ratio of deviatoric shear stress to deviatoric and lithospheric normal stress for mechanical coupling (χ) of (a) 0, (b) 0.05, (c) 0.10, and (d) 0.15. Heavy red and black lines mark ridge segments and transforms, respectively. For higher values of χ, fault orientations correlate strongly with the structural orientations of the Tasmantids, suggesting their morphology is substantially controlled by this inheritance.

Tasman Sea spreading center. Seamounts in different tectonic settings show distinct patterns in the orientations of volcanic rift zones and elongation axes, and widespread Bouguer gravity highs broadly share these orientations, suggesting they may reflect the edifices' magma plumbing systems. These trends align closely with principal stress directions predicted by Behn et al. (2002) for a spreading center with significant mechanical coupling across transforms ($\chi = 0.10–0.15$; Figure 12). This level of coupling is more likely at slow spreading systems like the Tasman Sea and is consistent with the complex, asymmetric faulting regimes commonly observed at inside and outside corners of such regimes, with the high variability attributed to the delicate balance between magmatic and amagmatic strain (Behn et al., 2002; Bird et al., 2002; Buck et al., 2005).

Across the chain, T_e is also substantially lower than expected, plotting predominantly on or above the 150° C isotherm with no clear age progression. Reduced T_e values are often explained using viscoelastic relaxation, but this reduction is usually more modest and the T_e values should retain a clear correlation with age at loading (e.g., Lambeck & Nakiboglu, 1981; Watts, 1978; Zhong & Watts, 2013). Similar very low isotherms are associated with seamount provinces that backtrack into the South Pacific Isotopic and Thermal Anomaly, such as the Cook-Austral Islands and the Magellan Seamounts (Figure 11; e.g., Calmant & Cazenave, 1987; Maia & Arkani-Hamed, 2002; Smith et al., 1989). Montelli et al. (2006) find slow P-wave and S-wave velocities in the upper mantle beneath Tasmania and the southern Tasman Sea, which they describe as consistent with a dying plume. The isotopic data available for the onshore East Australian volcanic chain show elevated ^{208}Pb/^{204}Pb and ^{207}Pb/^{204}Pb, consistent with the DUPAL anomaly and South Pacific Isotopic and Thermal Anomaly (Ewart, 1982). No Pb isotope data are available for the Tasmantids, but Sr, Nd, and trace element results are similar to those for the East Australian chain (Eggins et al., 1991). It thus is possible that a similar cause contributes to the low T_e values along the Tasmantids.

The faulting that influences the morphology may also influence the T_e. Fracture zones and highly extended continental crust, settings where brittle faulting is expected to dominate, consistently yield very low T_e estimates. This suggests seamount emplacement in these settings resulted in yielding-dominated deformation, and hence a reduced T_e (Watts & Burov, 2003). Seamounts on outside corners, where relatively little faulting is expected, dominate the highest T_e values. However, the low T_e associated with midsegment seamounts does not fit this model, which would predict that the strongest lithosphere would occur in these comparatively unfaulted regions, but midsegment seamounts are also generally the smallest in the Tasmantid chain. T_e is more difficult to constrain with modest flexural deflections, so these low results may not be robust.

Together, the seamount morphology and mode of isostatic compensation suggest a spreading ridge characterized by deep, pervasive faulting that remained apparently unhealed >20 Ma later. Thus, conical seamounts tend to occur midsegment or at outside corners, where the density of faulting is expected to be reduced, explaining their more conventional morphology. Rugged seamounts, with highly variable T_e and inherited structural patterns, are more common on inside corners and spanning multiple settings on short ridge segments, regions where brittle deformation is expected to be strong. Terraced seamounts are most commonly found on fracture zones, but are also characterized by their large size and elongate footprint. One possible explanation for this is melt focusing along a permeability barrier at the base of the thermal boundary layer (Montési et al., 2011). Although the barrier would be expected to deepen and flatten with time, enough 3-D topography could remain to affect the rising magma. A reduction in plate velocity (Knesel et al., 2008) or strengthening of the Tasmantid thermal anomaly could also increase volume, and small-scale convection could affect both elongation and distribution of edifices perpendicular to plate motion (Ballmer et al., 2011). The unique morphology of Cato can be attributed to its emplacement on the Kenn or Chesterfield Plateau, a drowned continental fragment (Colwell et al., 2010; Exon et al., 2006).

Why does the Tasman Sea lithosphere remain so weak, with yielding apparently still occurring on 20 Ma old faults? There is little evidence that this is the norm for oceanic lithosphere generated at slow-spreading ridges. Cochran (1979) and Kalnins and Watts (2010) found T_e at spreading ridges generally increases with decreasing spreading rate, and seamounts in the slow-spreading Atlantic generally plot within the standard 300–600° C isotherms in global compendia (e.g., Calmant & Cazenave, 1987; Watts et al., 2006), although low T_e for age has been observed at individual seamounts (e.g., Goodwillie & Watts, 1993; Minshull & Brozena, 1997). However, the Tasmantids are not just on slow-spreading lithosphere, they are also emplaced across the extinct mid-ocean ridge itself. As the ridge system shut down, the cessation of melt production and extension may not have been perfectly synchronous. An increase in amagmatic strain at the very end of spreading may explain the strong influence of spreading-related faulting on magma pathways and lithospheric strength >20 Ma later. This could be tested by future studies of T_e in ultraslow-spreading regions dominated by amagmatic extension. Inherited planes of weakness may also serve to reduce the critical yield stress of oceanic lithosphere entering a subduction zone, changing the overall force balance on the plate (Buffett, 2006). The effect of heterogeneous plate yield stress on subduction dynamics has not been investigated in detail but may help to explain the range of subduction behavior observed globally and may also be important in subduction initiation (e.g., Gurnis et al., 2004).

6. Conclusions

In this study, we combine shiptrack gravity, bathymetry, and dredge data collected during voyage TMD2012 (ss2012_v07) of the R/V *Southern Surveyor* with publicly available gravity and bathymetry data sets to analyze the morphology, structure, and evolution of the Tasmantid Seamount Chain.

We identify four morphological classes of seamount, which are correlated with their tectonic setting relative to the extinct Tasman Sea spreading center: (1) large, elongated, terraced guyots; (2) rugged seamounts; (3) conical seamounts; and (4) shield seamounts. Both terraced and rugged seamounts are predominantly found in settings with strong brittle deformation, such as fracture zones and inside corners, and characterized by generally low to intermediate T_e and strong preferential directions for structural trends. The larger volumes and elongated shape of the terraced seamounts may be explained by changing plate velocities or the 3-D topography of the melt permeability barrier. Conical seamounts, which typically have a near-circular footprint and intermediate to comparatively high T_e, are generally found midsegment and at outside corners, where faulting is less pervasive. The single shield seamount, Cato, is emplaced on thinned continental crust and characterized by gentle gradients and fields of small volcanic cones. Gravity reduction suggests Wreck, a terraced seamount, may also be underlain by continental crust; the morphological differences may reflect different degrees of thinning or melt focusing.

The tectonic control, high densities and dense cores required by gravity modeling, and low rates of mass wasting all indicate high intrusive:extrusive ratios and comparatively sluggish magma extraction. This combined with the length of the chain and comparatively modest subsidence points to a long-lived but relatively weak thermal anomaly.

Structural inheritance has long been considered an important control on the distribution and style of continental volcanoes, but is rarely invoked in the oceans due to the simpler, more homogenous structure and shorter tectonic history of oceanic lithosphere. However, the Tasmantids demonstrate that structural differences between fracture zone, inside corner, outside corner, midsegment, and on-axis settings can strongly influence the style, orientation, and location of oceanic intraplate volcanism for millions of years, particularly at slow-spreading ridges where limited magma supply enhances fault density and depth.

References

BODC (2014). The GEBCO_2014 Grid, version 20150318. Retrieved from https://www.gebco.net.

Ballmer, M. D., Ito, G., van Hunen, J., & Tackley, P. J. (2011). Spatial and temporal variability in Hawaiian hotspot volcanism induced by small-scale convection. *Nature Geoscience*, *4*(7), 457–460. https://doi.org/10.1038/ngeo1187

Beaman, R. J. (2010). Project 3DGBR: A high-resolution depth model for the Great Barrier Reef and Coral Sea (Marine and Tropical Sciences Research Facility Project 2.5i.1a Final Report pp.13.).

Behn, M., Lin, J., & Zuber, M. (2002). Evidence for weak oceanic transform faults. *Geophysical Research Letters*, *29*(24), 2207. https://doi.org/10.1029/2002GL015612

Bird, P., Kagan, Y. Y., & Jackson, D. D. (2002). Plate tectonics and earthquake potential of spreading ridges and oceanic transform faults. In S. Stein & J. T. Freymueller (Eds.), *Plate Boundary Zones, Geodynamics Series* (Vol. 30, pp. 203–218): American Geophysical Union. https://doi.org/10.1029/GD030p0203

Buck, W. R., Lavier, L. L., & Poliakov, A. N. B. (2005). Modes of faulting at mid-ocean ridges. *Nature*, *434*, 719–723.

Buffett, B. A. (2006). Plate force due to bending at subduction zones. *Journal of Geophysical Research*, *111*, 1–9. https://doi.org/10.1029/2006JB004295

Calmant, S., & Cazenave, A. (1987). Anomalous elastic thickness of the ocean lithosphere in the South-Central Pacific. *Nature*, *328*(6127), 236–238.

Chaytor, J. D., Keller, R. A., Duncan, R. A., & Dziak, R. P. (2007). Seamount morphology in the Bowie and Cobb hot spot trails, Gulf of Alaska. *Geochemistry, Geophysics, Geosystems*, *8*, Q09016. https://doi.org/10.1029/2007GC001712

Christensen, N. I., & Stanley, D. (2003). Seismic velocities and densities of rocks. In W. Lee, H. Kanamori, P. Jennings, & C. Kisslinger (Eds.), *International Handbook of Earthquake and Engineering Seismology, International Geophysics* (Vol. 81, pp. 1587–1594): Academic Press. https://doi.org/10.1016/S0074-6142(03)80278-4

Cochran, J. R. (1979). Analysis of isostasy in the world's oceans: 2. Midocean ridge crests. *Journal of Geophysical Research*, *84*(B9), 4713–4729.

Cohen, B. E. (2012). Tasmantid Seamounts: Volcanic, tectonic and carbonate record, MNF Voyage Summary, (pp. 1–27).

Cohen, B. E., Knesel, K. M., Vasconcelos, P. M., & Schellart, W. P. (2013). Tracking the Australian plate motion through the Cenozoic: Constraints from ^{40}Ar/^{39}Ar geochronology. *Tectonics*, *32*, 1371–1383. https://doi.org/10.1002/tect.20084

Colwell, J., Hashimoto, T., Rollet, N., Higgins, K., Bernardel, G., & McGiveron, S. (2010). Interpretation of seismic data, Capel and Faust Basins, Australia's remote offshore eastern frontier. *Geoscience Australia Record*, *2010*, 6.

Contreras-Reyes, E., Grevemeyer, I., Watts, A. B., Planert, L., Flueh, E. R., & Peirce, C. (2010). Crustal intrusion beneath the Louisville hotspot track. *Earth and Planetary Science Letters*, *289*(3-4), 323–333. https://doi.org/10.1016/j.epsl.2009.11.020

Crossingham, T. J., Vasconcelos, P. M., Cunningham, T., & Knesel, K. M. (2017). ^{40}Ar/^{39}Ar geochronology and volume estimates of the Tasmantid Seamounts: Support for a change in the motion of the Australian plate (Vol. 343, pp. 95–108). https://doi.org/10.1016/j.jvolgeores.2017.06.014

Czarnota, K., Hoggard, M. J., White, N., & Winterbourne, J. (2013). Spatial and temporal patterns of Cenozoic dynamic topography around Australia. *Geochemistry, Geophysics, Geosystems*, *14*, 634–658. https://doi.org/10.1029/2012GC004392

Czarnota, K., Roberts, G. G., White, N. J., & Fishwick, S. (2014). Spatial and temporal patterns of Australian dynamic topography from River Profile Modeling. *Journal of Geophysical Research: Solid Earth*, *119*, 1384–1424. https://doi.org/10.1002/2013JB010436

Davies, D. R., Rawlinson, N., Iaffaldano, G., & Campbell, I. H. (2015). Lithospheric controls on magma composition along Earth's longest continental hotspot track. *Nature*, *525*(7570), 511–514. https://doi.org/10.1038/nature14903

DiCaprio, L., Müller, R. D., & Gurnis, M. (2010). A dynamic process for drowning carbonate reefs on the northeastern Australian margin. *Geology*, *38*(1), 11–14. https://doi.org/10.1130/G30217.1

Dick, H. J. B., Lin, J., & Schouten, H. (2003). An ultraslow-spreading class of ocean ridge. *Nature*, *426*(6965), 405–412. https://doi.org/10.1038/nature02128

Ebinger, C. J., & Sleep, N. H. (1998). Cenozoic magmatism throughout east Africa resulting from impact of a single plume. *Nature*, *395*(6704), 788–791. https://doi.org/10.1038/27417

Eggins, S. M., Green, D. H., & Falloon, T. J. (1991). The Tasmantid Seamounts: Shallow melting and contamination of an EM1 mantle plume. *Earth and Planetary Science Letters*, *107*(3-4), 448–462. https://doi.org/10.1016/0012-821X(91)90092-V

Ewart, A. (1982). Petrogenesis of the Tertiary anorogenic volcanic series of Southern Queensland, Australia, in the light of trace element geochemistry and O, Sr and Pb isotopes. *Journal of Petrology*, *23*(3), 344–382.

Exon, N., Bernardel, G., Brown, J., Cortese, A., Findlay, C., Hoffmann, K., et al. (2006). The geology of the Mellish Rise region off northeast Australia: A key piece in a tectonic puzzle. *Geoscience Australia Record*, *2006*(8), 212.

Exon, N. F., Hill, P. J., Lafoy, Y., Heine, C., & Bernardel, G. (2006). Kenn Plateau off northeast Australia: A continental fragment in the southwest Pacific jigsaw. *Australian Journal of Earth Sciences*, *53*(4), 541–564.

Fornari, D. J., Moore, J. G., & Calk, L. (1979). A large submarine sand-rubble flow on Kilauea volcano, Hawaii. *Journal of Volcanology and Geothermal Research*, *5*(3-4), 239–256. https://doi.org/10.1016/0377-0273(79)90018-0

Gaina, C., Müller, R. D., Royer, J.-Y., & Symonds, P. (1999). Evolution of the Louisiade triple junction. *Journal of Geophysical Research*, *104*(B6), 12927. https://doi.org/10.1029/1999JB900038

Gaina, C., Roest, W. R., Müller, R. D., & Symonds, P. (1998). The opening of the Tasman Sea: A gravity anomaly animation. *Earth Interactions*, *2*(4), 1–23.

Gallart, J., Driad, L., Charvis, P., Sapin, M., Hirn, A., Diaz, J., et al. (1999). Perturbation to the lithosphere along the hotspot track of La Rèunion from an offshore-onshore seismic transect. *Journal of Geophysical Research*, *104*(B2), 2895–2908. https://doi.org/10.1029/98JB02840

Gee, M. J. R., Watts, A. B., Masson, D. G., & Mitchell, N. C. (2001). Landslides and the evolution of El Hierro in the Canary Islands. *Marine Geology*, *177*(3-4), 271–293. https://doi.org/10.1016/S0025-3227(01)00153-0

Goodwillie, A. M., & Watts, A. B. (1993). An altimetric and bathymetric study of elastic thickness in the Central Pacific Ocean. *Earth and Planetary Science Letters*, *118*(1-4), 311–326.

Gurnis, M., Hall, C., & Lavier, L. (2004). Evolving force balance during incipient subduction. *Geochemistry, Geophysics, Geosystems*, *5*, Q07001. https://doi.org/10.1029/2003GC000681

Hekinian, R., Stoffers, P., Ackermand, D., Rèvillon, S., Maia, M., & Bohn, M. (1999). Ridge-hotspot interaction: The Pacific-Antarctic Ridge and the Foundation Seamounts. *Marine Geology*, *160*(3-4), 199–223. https://doi.org/10.1016/S0025-3227(99)00027-4

Hill, P. (1994). Geology and geophysics of the offshore Maryborough, Capricorn and northern Tasman Basins: Results of AGSO Survey 91. *AGSO Record*, *1994*(1), 71.

Huppert, K. L., Royden, L. H., & Perron, J. T. (2015). Dominant influence of volcanic loading on vertical motions of the Hawaiian Islands. *Earth and Planetary Science Letters*, *418*, 149–171. https://doi.org/10.1016/j.epsl.2015.02.027

Jilinski, P., Fontes, S. L., & Meju, M. A. (2013). Estimating optimum density for regional Bouguer reduction by morphological correlation of gravity and bathymetric maps: Examples from offshore south-eastern Brazil. *Geo-Marine Letters*, *33*(1), 67–73. https://doi.org/10.1007/s00367-012-0312-0

Johnson, R. W., Knutson, J., & Taylor, S. R. (1989). *Intraplate volcanism in eastern Australia and New Zealand*. Cambridge, UK: Cambridge University Press.

Kalnins, L. M., Cohen, B. E., Fitton, J. G., Mark, D., Mark, F. D., & Barfod, D. (2015). The East Australian, Tasmantid, and Lord Howe Volcanic Chains: Possible mechanisms behind a trio of hotspot trails, in: AGU Fall Meeting Abstracts, DI41A–2591.

Kalnins, L. M., & Watts, A. B. (2009). Spatial variations in effective elastic thickness in the Western Pacific Ocean and their implications for Mesozoic volcanism. *Earth and Planetary Science Letters*, *286*(1-2), 89–100. https://doi.org/10.1016/j.epsl.2009.06.018

Kalnins, L. M., & Watts, A. B. (2010). Exploring the strength of newly formed oceanic lithosphere and its correlation with spreading rate and ridge depth anomalies, in: AGU Fall Meeting Abstracts, V11A-2253.

Keene, J., Baker, C., Tran, M., & Potter, A. (2008). Sedimentology and geomorphology of the East Marine region of Australia: A spatial analysis. *Geoscience Australia Record*, *2008*(10), 262.

Kim, S. S., & Wessel, P. (2010). Flexure modelling at seamounts with dense cores. *Geophysical Journal International*, *182*, 583–598. https://doi.org/10.1111/j.1365-246X.2010.04653.x

Klügel, A., Longpré, M.-A., Stix, J., et al. (2015). Deep intrusions, lateral magma transport and related uplift at ocean island volcanoes. *Earth and Planetary Science Letters*, *431*, 140–149.

Knesel, K. M., Cohen, B. E., Vasconcelos, P. M., & Thiede, D. S. (2008). Rapid change in drift of the Australian plate records collision with Ontong Java plateau. *Nature*, *454*(7205), 754–757. https://doi.org/10.1038/nature07138

Kokelaar, P. (1986). Magma-water interactions in subaqueous and emergent basaltic volcanism. *Bulletin of Volcanology*, *48*(5), 275–289.

Kongsberg Maritime AS (2004). EM 300 Multibeam Echo Sounder Maintenance Manual.

Koppers, A. A. P., Yamazaki, T., Geldmacher, J., Gee, J. S., Pressling, N., Hoshi, H., et al. (2012). Limited latitudinal mantle plume motion for the Louisville hotspot. *Nature Geoscience*, *5*, 911–917. https://doi.org/10.1038/NGEO1638

Lambeck, K., & Nakiboglu, S. M. (1981). Seamount loading and stress in the ocean lithosphere: 2. Viscoelastic and elastic-viscoelastic models. *Journal of Geophysical Research*, *86*(B8), 6961. https://doi.org/10.1029/JB086iB08p06961

Le Gonidec, Y., Lamarche, G., & Wright, I. C. (2003). Inhomogeneous substrate analysis using EM300 backscatter imagery. *Marine Geophysical Research*, *24*(3-4), 311–327. https://doi.org/10.1007/s11001-004-1945-9

Le Pichon, X., & Talwani, M. (1964). Gravity survey of a seamount near 35°N 46°W in the North Atlantic. *Marine Geology*, *2*(4), 262–277.

Lee, T.-G., Moon, J.-W., & Jung, M.-S. (2009). Three-dimensional flexure modelling of seamounts near the Ogasawara Fracture Zone in the western Pacific. *Geophysical Journal International*, *177*, 247–258. https://doi.org/10.1111/j.1365-246X.2008.04054.x

Lynch, M. A. (1999). Linear ridge groups: Evidence for tensional cracking in the Pacific Plate. *Journal of Geophysical Research*, *104*(B12), 29321–29333.

Maia, M., & Arkani-Hamed, J. (2002). The support mechanism of the young Foundation Seamounts inferred from bathymetry and gravity. *Geophysical Journal International*, *149*(1), 190–210.

McDougall, I., & Duncan, R. A. (1988). Age progressive volcanism in the Tasmantid Seamounts. *Earth Planetary Science Letters*, *89*, 207–220.

McKenzie, D., Jackson, J., & Priestley, K. (2005). Thermal structure of oceanic and continental lithosphere. *Earth Planetary Science Letters*, *233*(3-4), 337–349. https://doi.org/10.1016/j.epsl.2005.02.005

Michon, L., Saint-Ange, F., Bachelery, P., Villeneuve, N., & Staudacher, T. (2007). Role of the structural inheritance of the oceanic lithosphere in the magmato-tectonic evolution of Piton de la Fournaise volcano (La Réunion Island). *Journal of Geophysical Research*, *112*, B04205. https://doi.org/10.1029/2006JB004598

Minshull, T. A., & Brozena, J. M. (1997). Gravity anomalies and flexure of the lithosphere at Ascension Island. *Geophysical Journal International*, *131*(2), 347–360. https://doi.org/10.1111/j.1365-246X.1997.tb01227.x

Mitchell, N. C., Masson, D. G., Watts, A. B., Gee, M. J. R., & Urgeles, R. (2002). The morphology of the submarine flanks of volcanic ocean islands: A comparative study of the Canary and Hawaiian hotspot islands. *Journal of Volcanology and Geothermal Research*, *115*(1-2), 83–107. https://doi.org/10.1016/S0377-0273(01)00310-9

Montelli, R., Nolet, G., Dahlen, F., & Masters, G. (2006). A catalogue of deep mantle plumes: New results from finite-frequency tomography. *Geochemistry, Geophysics, Geosystems*, *7*, Q11007. https://doi.org/10.1029/2006GC001248

Montési, L. G. J., Behn, M. D., Hebert, L. B., Lin, J., & Barry, J. L. (2011). Controls on melt migration and extraction at the ultraslow Southwest Indian Ridge 10°–16°E. *Journal of Geophysical Research*, *116*(10), B10102. https://doi.org/10.1029/2011JB008259

Moore, J. G., Clague, D. A., Holcomb, R. T., Lipman, P. W., Normark, W. R., & Torresan, M. E. (1989). Prodigious submarine landslides on the Hawaiian Ridge. *Journal of Geophysical Research*, *94*(B12), 17465–17484. https://doi.org/10.1029/JB094iB12p17465

Mortimer, N., Campbell, H. J., Tulloch, A. J., King, P. R., Stagpoole, V. M., Wood, R. A., et al. (2017). Zealandia: Earth's hidden continent. *GSA Today*, *27*(3), 27–35. https://doi.org/10.1130/GSATG321A.1

Müller, R. D., Sdrolias, M., Gaina, C., & Roest, W. R. (2008). Age, spreading rates, and spreading asymmetry of the world's ocean crust. *Geochemistry, Geophysics, Geosystems*, *9*, Q04006. https://doi.org/10.1029/2007GC001743

Mutter, J. C. (1974). *Geophysical results from the Coral Sea: continental margins survey report*. Australian Bureau of Mineral Resources, Geology, and Geophysics. Retrieved from https://data.gov.au/dataset/geophysical-results-from-the-coral-sea-continental-margins-survey-report

O'Connor, J. M., Hoernle, K., Müller, R. D., Morgan, J. P., Butterworth, N. P., Hauff, F., et al. (2015). Deformation-related volcanism in the Pacific Ocean linked to the Hawaiian–Emperor bend. *Nature Geoscience*, *8*(5), 393.

FROGTECH (2014). *Phanerozoic OZ SEEBASE v2*. Canberra Australia: Frogtech Geoscience.

Parker, R. L. (1973). The rapid calculation of potential anomalies. *Geophysical Journal of the Royal Astronomical Society*, *31*, 447–455.

Paulatto, M., Watts, A. B., & Peirce, C. (2014). Potential field and bathymetric investigation of the Monowai volcanic centre, Kermadec Arc: Implications for caldera formation and volcanic evolution. *Geophysical Journal International*, *197*, 1484–1499. https://doi.org/10.1093/gji/ggt512

Ramalho, R. S., Brum da Silveira, A., Fonseca, P. E., Madeira, J., Cosca, M., Cachão, M., et al. (2015). The emergence of volcanic oceanic islands on a slow-moving plate: The example of Madeira Island, NE Atlantic. *Geochemistry, Geophysics, Geosystems*, *16*, 522–537. https://doi.org/10.1002/2014GC005657

Ramalho, R., Helffrich, G., Cosca, M., Vance, D., Hoffmann, D., & Schmidt, D. (2010). Episodic swell growth inferred from variable uplift of the Cape Verde hotspot islands. *Nature Geoscience*, *3*(11), 774–777.

Ramalho, R. S., Quartau, R., Trenhaile, A. S., Mitchell, N. C., Woodroffe, C. D., & Ávila, S. P. (2013). Coastal evolution on volcanic oceanic islands: A complex interplay between volcanism, erosion, sedimentation, sea-level change and biogenic production. *Earth-Science Reviews*, *127*, 140–170. https://doi.org/10.1016/j.earscirev.2013.10.007

Richards, M., Contreras-Reyes, E., Lithgow-Bertelloni, C., Ghiorso, M., & Stixrude, L. (2013). Petrological interpretation of deep crustal intrusive bodies beneath oceanic hotspot provinces. *Geochemistry, Geophysics, Geosystems*, *14*, 604–619. https://doi.org/10.1029/2012GC004448

Sandwell, D. T., Müller, R. D., Smith, W. H. F., Garcia, E., & Francis, R. (2014). New global marine gravity model from CryoSat-2 and Jason-1 reveals buried tectonic structure. *Science (80-)*, *346*(6205), 65–67. https://doi.org/10.1126/science.1258213

Sandwell, D. T., & Smith, W. H. F. (2009). Global marine gravity from retracked Geosat and ERS-1 altimetry: Ridge segmentation versus spreading rate. *Journal of Geophysical Research*, *114*, B01411. https://doi.org/10.1029/2008JB006008

Sandwell, D. T., Winterer, E. L., Mammerickx, J., Duncan, R. A., Lynch, M. A., Levitt, D. A., & Johnson, C. L. (1995). Evidence for diffuse extension of the Pacific plate from Pukapuka Ridges and cross-grain gravity lineations. *Journal of Geophysical Research*, *100*(B8), 15087–15099.

Seton, M., Müller, R. D., Zahirovic, S., Gaina, C., Torsvik, T., Shephard, G., et al. (2012). Global continental and ocean basin reconstructions since 200 Ma. *Earth-Science Reviews*, *113*(3-4), 212–270.

Shaw, R. (1979). On the evolution of the Tasman Sea and adjacent continental margins (PhD thesis). University of Sydney.

Smith, W. H. F., Staudigel, H., Watts, A. B., & Pringle, M. S. (1989). The Magellan Seamounts – Early Cretaceous record of the South-Pacific isotopic and thermal anomaly. *Journal of Geophysical Research*, *94*(B8), 10501–10523. https://doi.org/10.1029/JB094iB08p10501

Symonds, P. (1973). The structure of the North Tasman Sea. *BMR Record*, *1973*(167), 1–23.

Tarduno, J. A., Duncan, R. A., Scholl, D. W., Cottrell, R. D., Steinberger, B., Thordarson, T., et al. (2003). The Emperor Seamounts: Southward motion of the Hawaiian hotspot plume in Earth's mantle. *Science*, *301*(5636), 1064–1069. https://doi.org/10.1126/science.1086442

Turcotte, D. L., & Schubert, G. (2002). *Geodynamics* (2nd ed). Cambridge: Cambridge University Press.

Valentine, G., & Krogh, K. (2006). Emplacement of shallow dikes and sills beneath a small basaltic volcanic center – The role of pre-existing structure (Paiute Ridge, southern Nevada, USA). *Earth Planetary Science Letters*, *246*(3-4), 217–230. https://doi.org/10.1016/j.epsl.2006.04.031

Watts, A. B. (1978). An analysis of isostasy in the world's oceans 1. Hawaiian-Emperor Seamount Chain. *Journal of Geophysical Research*, *83*(B12), 5989–6004. https://doi.org/10.1029/JB083iB12p05989

Watts, A. B. (1988). Gravity-anomalies, crustal structure and flexure of the lithosphere at the Baltimore Canyon Trough. *Earth and Planetary Science Letters*, *89*(2), 221–238.

Watts, A. B., & Burov, E. B. (2003). Lithospheric strength and its relationship to the elastic and seismogenic layer thickness. *Earth Planetary Science Letters*, *213*(1-2), 113–131. https://doi.org/10.1016/S0012-821X(03)00289-9

Watts, A. B., Sandwell, D. T., Smith, W. H. F., & Wessel, P. (2006). Global gravity, bathymetry, and the distribution of submarine volcanism through space and time. *Journal of Geophysical Research*, *111*, 1–26. https://doi.org/10.1029/2005JB004083

Watts, A. B., & Zhong, S. (2000). Observations of flexure and the rheology of oceanic lithosphere. *Geophysical Journal International*, *142*(3), 855–875. https://doi.org/10.1046/j.1365-246X.2000.00189.x

Weigel, W., & Grevemeyer, I. (1999). The Great Meteor seamount: Seismic structure of a submerged intraplate volcano. *Journal of Geodynamics*, *28*(1), 27–40. https://doi.org/10.1016/S0264-3707(98)00030-1

Wessel, P. (1993). Observational constraints on models of the Hawaiian hot spot swell. *Journal of Geophysical Research*, *98*(93), 95–104. https://doi.org/10.1029/93JB01230

Wessel, P., Sandwell, D., & Kim, S.-S. (2010). The global seamount census. *Oceanography*, *23*(1), 24–33. https://doi.org/10.5670/oceanog.2010.60

Wessel, P., & Smith, W. (2013). Generic Mapping Tools: Improved version released. *Eos (Washington. DC)*, *94*(45), 409–10.

Whittaker, J. M., Goncharov, A., Williams, S. E., Müller, R. D., & Leitchenkov, G. (2013). Global sediment thickness data set updated for the Australian-Antarctic Southern Ocean. *Geochemistry, Geophysics, Geosystems*, *14*, 3297–3305. https://doi.org/10.1002/ggge.20181

Winterbourne, J., White, N., & Crosby, A. (2014). Accurate measurements of residual topography from the oceanic realm. *Tectonics*, *33*, 982–1015. https://doi.org/10.1002/2013TC003372

Zhong, S., & Watts, A. B. (2013). Lithospheric deformation induced by loading of the Hawaiian Islands and its implications for mantle rheology. *Journal of Geophysical Research: Solid Earth*, *118*, 6025–6048. https://doi.org/10.1002/2013JB010408